JGR Solid Earth

RESEARCH ARTICLE
10.1029/2020JB020820

Characteristics of Frequent Dynamic Triggering of Microearthquakes in Southern California

Wenyuan Fan[1], Andrew J. Barbour[2], Elizabeth S. Cochran[3], and Guoqing Lin[4]

[1]Scripps Institution of Oceanography, U.C. San Diego, La Jolla, CA, USA, [2]Earthquake Science Center, U.S. Geological Survey, Moffett Field, CA, USA, [3]Earthquake Science Center, U.S. Geological Survey, Pasadena, CA, USA, [4]Rosenstiel School of Marine and Atmospheric Science, University of Miami, Miami, FL, USA

Key Points:

- Distant earthquakes frequently trigger local microearthquakes in Southern California
- Both instantaneous and delayed-dynamic triggering occur in the region
- Nonlinear triggering processes likely dominate the observed cases

Supporting Information:

- Supporting Information S1

Correspondence to:
W. Fan,
wenyuanfan@ucsd.edu

Citation:
Fan, W., Barbour, A. J., Cochran, E. S., & Lin, G. (2021). Characteristics of frequent dynamic triggering of microearthquakes in Southern California. *Journal of Geophysical Research: Solid Earth*, *126*, e2020JB020820. https://doi.org/10.1029/2020JB020820

Received 20 AUG 2020
Accepted 3 DEC 2020

Abstract Dynamic triggering of earthquakes has been reported at various fault systems. The triggered earthquakes are thought to be caused either directly by dynamic stress changes due to the passing seismic waves, or indirectly by other nonlinear processes that are initiated by the passing waves. Distinguishing these physical mechanisms is difficult because of the general lack of high-resolution earthquake catalogs and robust means to quantitatively evaluate triggering responses, particularly, delayed responses. Here we use the high-resolution Quake Template Matching catalog in Southern California to systematically evaluate teleseismic dynamic triggering patterns in the San Jacinto Fault Zone and the Salton Sea Geothermal Field from 2008 to 2017. We develop a new statistical approach to identify triggered cases, finding that approximately 1 out of every 5 global $M_w \geq 6$ earthquakes dynamically trigger microearthquakes in Southern California. The triggering responses include both instantaneous and delayed triggering, showing a highly heterogeneous pattern and indicating possible evolving triggering thresholds. We do not observe a clear peak ground velocity triggering threshold that can differentiate triggering earthquakes from nontriggering events, but there are subtle differences in the frequency content of the ground motion that may differentiate the earthquakes. In contrast to the depth distribution of background seismicity, the identified triggered earthquakes tend to concentrate at the edges of the seismogenic zones. Although instantaneously triggered earthquakes are likely a result of dynamic Coulomb stress changes, the cases of delayed-dynamic triggering are best explained by nonlinear triggering processes, including cyclic material fatigue, accelerated transient creep, and stochastic frictional heterogeneities.

Plain Language Summary Earthquake-to-earthquake interaction and triggering are frequently observed at various fault systems. For example, large earthquakes can cause aftershocks in the near-field region by permanently altering the stress field, which is termed static earthquake triggering. Seismic waves from earthquakes can also trigger events on faults up to thousands of kilometers away. Such triggering processes are called dynamic triggering. At such great separation distances, the stress perturbation of dynamic triggering is commonly small, which is perplexing from a physical perspective. With a high-resolution earthquake catalog in Southern California, our study shows that local earthquakes are frequently triggered by remote earthquakes. The majority of these local earthquakes are triggered with a delayed response, sometimes occurring hours after the seismic wave passage. Our results suggest that seismic waves cause temporary disturbances in the underlying physical responses within the subsurface, with triggering thresholds that can change in both space and time.

1. Introduction

Earthquakes on separate faults can trigger and interact with each other (Freed, 2005; Hill & Prejean, 2015). Earthquakes triggered on receiver faults are often caused by the static and/or dynamic stress perturbations (Gomberg et al., 2001; Hill et al., 1993; King et al., 1994). The static triggering effects are most significant within a few fault lengths, while dynamic triggering can cause seismic events up to thousands of kilometers away (Harris, 1998; Velasco et al., 2008). Dynamic triggering due to passing seismic waves has been observed at various fault systems from near-field to far-field with stress perturbations ranging from ~1 MPa to ~0.1 kPa (e.g., Gomberg & Johnson, 2005; Kilb, 2003; van Der Elst & Brodsky, 2010). The large range of dynamic stress perturbations that can trigger earthquakes challenges our general understanding of earthquake failure initiation processes, particularly when triggering stresses are small. Understanding the role of

dynamic strain (stress) perturbations in earthquake triggering, including the initiation of possible secondary mechanisms caused by the transient dynamic strain fields, provides insight on earthquake nucleation and rupture physics that may ultimately impact seismic hazard mitigation (e.g., Harris et al., 2002; Kilb et al., 2000; Stein, 1999).

Dynamic triggering has been shown to influence the occurrence of earthquakes, aseismic slow earthquakes, tectonic tremors, landslides, and icequakes (Aiken et al., 2013; Gomberg et al., 1997; Gonzalez-Huizar et al., 2012; H. P. Johnson et al., 2017; Obara, 2002; Peng et al., 2014; Tymofyeyeva et al., 2019; Wallace et al., 2017). Triggered shallow crustal earthquakes occur at a variety of fault systems, including subduction zones, continental plate boundaries, and geothermal fields (Brodsky et al., 2003; Fan & Shearer, 2016; Kaven, 2020; Nissen et al., 2016; Velasco et al., 2008; Yun et al., 2019). For example, the 2012 M_w 8.6 Indian Ocean earthquake dynamically triggered earthquakes on a global scale (Pollitz et al., 2012). Observationally, dynamic triggering is a causal relationship inferred from correlations between the passing seismic waves and the occurrence of slip activities. The most compelling examples show the instantaneous occurrence of triggered earthquakes during the passing surface waves (Peng et al., 2009; Prejean et al., 2004; Velasco et al., 2008). In addition, delayed triggering has also been reported with an apparent onset of a local seismicity increase minutes to days after the passing seismic waves (Alfaro-Diaz et al., 2020; Brodsky, 2006; Fan & Shearer, 2016; Peña Castro et al., 2019; Peng et al., 2011; Shelly et al., 2011; van der Elst et al., 2013). In general, the observation of pervasively triggered earthquakes suggests that dynamic triggering may be a common process in causing earthquakes (Velasco et al., 2008), but the physical mechanisms controlling dynamic triggering processes remain poorly understood, particularly with cases of delayed triggering.

Southern California is a great natural laboratory to investigate earthquake dynamic triggering processes with high-quality earthquake catalogs and dense seismic and geodetic instrumentation. In addition to the main transform boundary delineated by the San Andreas fault, a complex network of faults accommodates a significant portion of the total plate motion. Consequently, seismicity rates in the region are high: 1.81 million earthquakes were detected from 2008 to 2017 (Ross et al., 2019). The most active fault zone within the larger plate boundary system is the San Jacinto Fault Zone (SJFZ) (Figure 1) (Plesch et al., 2007). Within the Salton Trough, active earthquake sequences at the Salton Sea Geothermal Field (SSGF) often occur in swarm-like clusters that sometimes show clear migration patterns (Chen & Shearer, 2011). Seismicity in this region generally shows characteristics deviating from typical tectonic earthquakes and reflecting possible imprints of local production and injection of geothermal fluids (e.g., Brodsky & Lajoie, 2013; Cheng & Chen, 2018; Crandall-Bear et al., 2018; Llenos & Michael, 2016; Zhang et al., 2017). Dynamically triggered seismicity has been reported in the region at both tectonically active faults (SJFZ) and faults within the SSGF area (e.g., Gomberg et al., 2001; Meng & Peng, 2014). The complex fault system, energetic seismicity, robust evidence of dynamic triggering, and dense instrumentation offer an opportunity to comprehensively examine earthquake dynamic triggering processes in the region.

Here, we evaluate the earthquake dynamic triggering processes in Southern California by first developing a new statistical approach to associate dynamically triggered local seismicity with teleseismic earthquakes. We then compute the peak ground velocities (PGV) and self-normalized velocity spectra to compare the triggering responses of different mainshocks at different fault segments; we use peak dynamic strain (PDS) from a cluster of borehole strainmeters in the Anza region to corroborate PGV for the SJFZ. Of the global $M_w \geq 6$ earthquakes that we tested from 2008 to 2017, over 20% of them dynamically triggered microearthquakes in Southern California. Some of the microearthquakes were triggered instantaneously, but the majority of them were triggered with a short delay. The triggering response varies by fault segments, but statistically the responses of faults in SSGF are similar to the faults in SJFZ. We find that neither PGV nor PDS can clearly differentiate triggering earthquakes from nontriggering events. However, the seismic waves of some triggering earthquakes are more enriched in low-frequency ground motion. We also observe that distant earthquakes from back-azimuthal directions of 60°–90° and 180°–210° are more likely to trigger earthquakes in Southern California. Furthermore, dynamically triggered earthquakes have depth distributions that deviate from the distributions of background seismicity by concentrating at the edges of the seismogenic zones. These observations suggest that linear dynamic triggering mechanisms are likely of

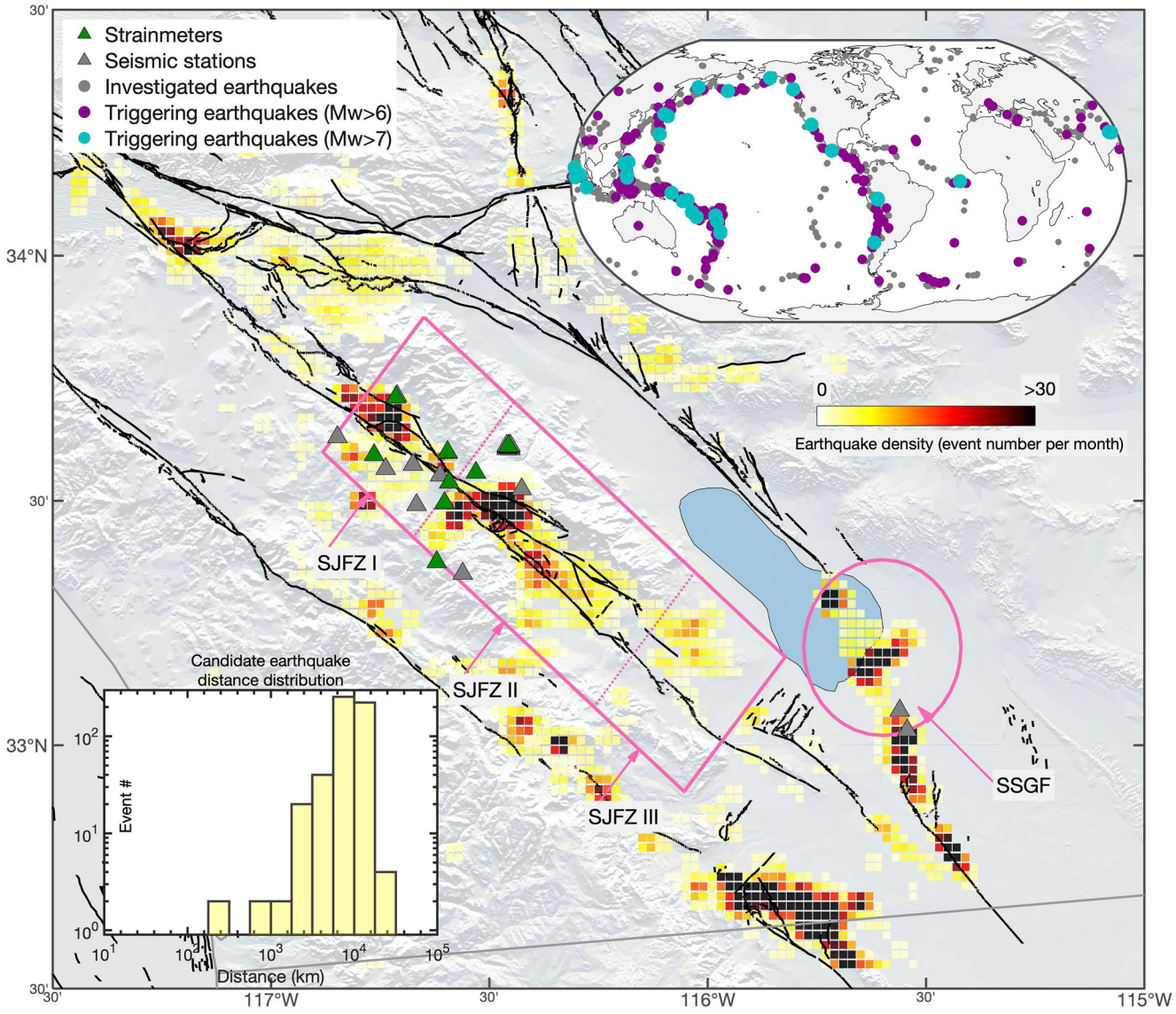

Figure 1. Faults in Southern California and seismicity rate in the San Jacinto Fault Zone (SJFZ) and the Salton Sea Geothermal Field (SSGF). The earthquakes are from the Quake Template Matching (QTM) catalog (Ross et al., 2019). We divide the San Jacinto Fault Zone into three along strike rectangular segments (SJFZ-I, II, and III) and investigate seismicity within 20 km of the Salton Sea Geothermal Field (SSGF). The gray and green triangles are the broadband seismic stations and strainmeters. The gray dots in the upper right insert are the globally distributed candidate triggering earthquakes ($M_w \geq 6.0$), and the color dots are distant earthquakes that have dynamically triggered microearthquakes in the SJFZ and/or the SSGF regions (Figure S1, Table S1). The lower left insert shows the distance distribution of the triggering and "twin" nontriggering earthquakes. The closest earthquake is 190 km away from the study regions.

secondary importance and the nonlinear mechanisms appear to dominate dynamic triggering processes in SJFZ and SSGF.

2. Datasets

2.1. Locally Triggered Earthquakes

We use the Quake Template Matching (QTM) catalog of Southern California seismicity (Ross et al., 2019) to investigate dynamic triggering in the San Jacinto Fault Zone (SJFZ) and Salton Sea Geothermal Field (SSGF). The QTM catalog is an automated product and is obtained with a template matching technique,

using templates from earthquakes that were reported in the Southern California Seismic Network (SCSN) catalog from 2000 to 2017 (Ross et al., 2019). The QTM catalog includes 1.81 million earthquakes from 2008 to 2017, containing 10 times more earthquakes than the original SCSN catalog, and the QTM catalog has an apparent magnitude of completeness as 0.3 (Ross et al., 2019). In this study, we use the 9.5dev version of the QTM catalog, which has a minimum detection threshold of 9.5 times the median absolute deviation (Ross et al., 2019). We only analyze earthquakes of $M \geq 0.3$ to assure the robustness of the identified dynamic triggering cases. We focus on the SJFZ and SSGF regions to understand spatial variations of the dynamic triggering processes. The comparison between the two regions may also shed light on differing triggering responses of natural faults and the ones in geothermal fields. Following Meng and Peng (2014), we divide the SJFZ into three rectangular segments along strike, SJFZ-I, SJFZ-II, and SJFZ-III with lengths of 30, 60, and 30 km, respectively; their widths are all 40 km centered across the fault. We also investigate seismicity within 20 km of the Salton Sea Geothermal Field (Figure 1). In total, there are ∼156 thousand microearthquakes in the regions of interest.

2.2. Triggering Sources

We consider all $M_w \geq 6.0$ earthquakes in the Global Centroid Moment Tensor Project (GCMT) catalog as potential triggering mainshocks (Ekström et al., 2012). In total, there are 1,313 candidate triggering earthquakes from 2008 to 2017. The 2010 M_w 7.2 El-Mayor Cucapah earthquake occurred within ∼300 km of the SJFZ and SSGF regions, which may have modulated seismicity rates in these areas, both dynamically and statically (Meng & Peng, 2014). To isolate the dynamic triggering responses of the seismicity in the regions, we do not consider candidate teleseismic earthquakes within 2 weeks after the 2010 El-Mayor Cucapah earthquake. Imposing this restriction leaves 1,306 candidate triggering earthquakes for detailed investigations.

2.3. Broadband Ground Motions

To characterize the local ground motions due to the teleseismic waves, we evaluate both the peak ground velocity and the velocity spectra. We download three-component velocity records of these earthquakes for all broadband stations within the SJFZ and SSGF regions from the Data Management Center (DMC) of the Incorporated Research Institutions for Seismology (IRIS). We download 2-h records starting 30 min before the theoretical *P*-wave arrivals of the candidate triggering earthquakes. The *P*-wave arrival times are calculated with the Preliminary Determination of Epicenters Bulletin location and the IASP91 velocity model with respect to a reference location in SJFZ (116.593°W, 33.537°N) (Kennett & Engdahl, 1991). After obtaining the data, we first remove the instrument responses and apply a data quality control procedure to remove noisy records. We bandpass filter the records from 0.01 to 0.05 Hz (20–100 s periods) with a fourth-order Butterworth filter and discard records with signal-to-noise ratios (SNR) less than five for these filtered records. We define the SNR as the root-mean-square (RMS) amplitude ratio of time windows 30 min before and 30 min after the theoretical *P*-wave arrivals. We then measure the peak ground velocity with the filtered records as detailed in Section 3.2. We also compute velocity spectra with unfiltered three-component velocity seismograms (Section 3.2). In total, we investigate records from 28 stations within the SJFZ and SSGF regions (Figure 1).

2.4. Dynamic Strains

We use dynamic strain records from the Anza borehole strainmeters to corroborate the PGV measurements. Dynamic strains from triggering earthquakes are rarely directly measured but mostly inferred from ground velocities assuming a planar wavefield, where strain and velocity are proportional through a phase velocity. The Anza section of the SJFZ is a unique study region because multiple strainmeters are either colocated or in very close proximity to some of the same broadband seismometers discussed above (Barbour & Agnew, 2012) (Figure 1). We follow a similar procedure in assembling the strain records as with the velocity data except that there is no instrument response to remove with data from these strainmeters: they have

linear sensitivity from static strain through the seismic band. Here the strain data have a sampling rate of 20 Hz.

3. Methods

3.1. Identifying Seismicity Rate Changes

3.1.1. Previous Methods and Their Limitations

The premise of earthquake dynamic triggering is that a measurable change in seismicity rate can be associated with the passing seismic waves. Thus, the key to identifying triggering cases is a robust characterization of seismicity rate changes. A few statistical approaches developed over the years seek to quantify the changes of seismicity rate by requiring that their statistic exceeds some threshold value(s) to be classified as a significant rate change (Aiken et al., 2018; Habermann, 1987; Matthews & Reasenberg, 1988; Pankow & Kilb, 2020). The β-statistic is the most widely used statistic to identify dynamic triggering cases (Delbridge et al., 2017; Marsan & Nalbant, 2005):

$$\beta = \frac{N_a - \Lambda}{\sqrt{\Lambda}} \tag{1}$$

where N_a is the number of earthquakes during the time period of interest (δt_a), and Λ is the expected number of events, which is computed from $\Lambda = N_b \frac{\delta t_a}{\delta t_b}$ with N_b as the number of events during a reference time period δt_b. The β-statistic measures the difference between the observed number of earthquakes N_a in δt_a and the expected number Λ, a background rate, relative to the expected variability in numbers of earthquakes in that time period. In the context of dynamic triggering, N_a typically refers to the number of earthquakes in a period after the posited triggering event, and N_b is the number of earthquakes in the period preceding the triggering earthquake. Often, N_b is a small value due to the short time window length, which can cause biases in the β-statistic estimations. Accordingly, β is positive when there is an increase in seismicity rate comparing to background levels, and it is negative when there is a decrease; $\beta \geq 2.0$ is typically considered an indicator of a seismicity increase at the 95% significance level (Marsan & Wyss, 2011).

Despite its popularity, using the β-statistic to identify dynamic triggering cases comes with a few limitations (Marsan & Nalbant, 2005; Pankow & Kilb, 2020). The statistic might not be robust when evaluating short time windows, so there can be a wide range of β for both triggering and nontriggering cases, with β-thresholds often larger than 2 (Cattania et al., 2017; Prejean & Hill, 2018). Perhaps, the $\beta \geq 2.0$ threshold is most critically challenged when only a small number of earthquakes are reported during the time window of interest (Marsan & Nalbant, 2005). This is because the threshold is valid assuming a large number of earthquakes, for which the Poisson distribution of earthquakes tends to a Gaussian law. Further, even when a catalog includes a large number of earthquakes, the Poisson distribution of earthquakes characterizes random processes while the dynamically triggering cases are clearly correlated phenomena. For such cases, the distribution of the β-statistic might be skewed from a Gaussian distribution making the commonly used metric $\beta \geq 2.0$ inadequate to capture the significance of a seismicity increase. To mitigate this limitation, methods measuring the probability of triggering (P), or alternative statistics like the Z-statistic and γ-statistic, have been proposed to improve the robustness of triggering detection (Aiken et al., 2018; Aron & Hardebeck, 2009; Marsan, 2003; Marsan & Nalbant, 2005). Nonetheless, they rely on assumptions of probability density function (PDF) that are difficult to validate when the physical mechanism of dynamic triggering are poorly understood.

3.1.2. A New Approach: Distributions of the β-Statistic

Here, we propose a method that is free from PDF assumptions and estimate probability distributions of the β-statistic by resampling the QTM catalog. The β-statistic of a time window after a teleseismic earthquake must exceed a probability threshold (e.g., 95% significance) when local earthquakes are considered dynamically triggered. The probability threshold is obtained from the estimated distribution (denoted by distribution-$\mathcal{N}_a$) (Figure 2). More specifically, our procedure is detailed as follows:

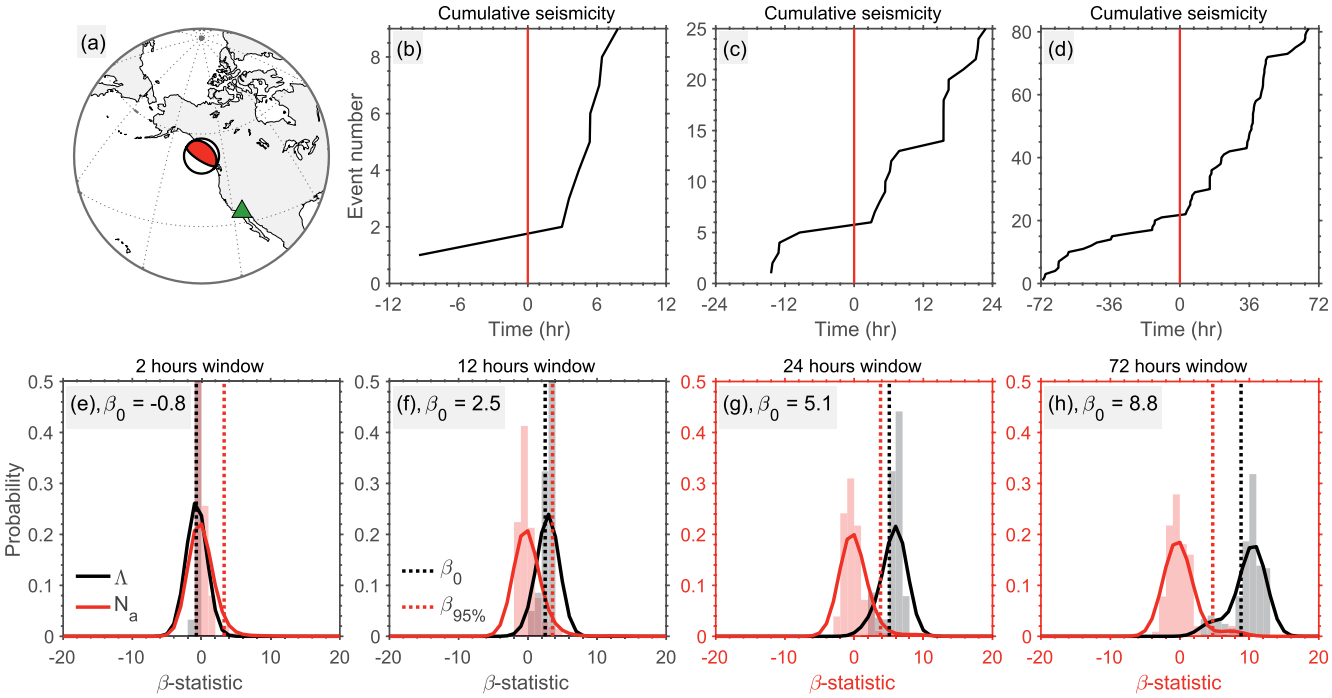

Figure 2. The 2012 M_w 7.8 Haida Gwaii earthquake and the dynamic triggering responses in the SJFZ-I region during the 2-, 12-, 24-, and 72-h time windows. (a), location and the focal mechanism of the 2012 Haida Gwaii earthquake. The green triangle shows the study region. (b–d), cumulative seismicity. The *P*-wave arrival time is denoted at time 0, showing as the red line. (e–h), β-statistic distributions. Distribution-$\mathcal{N}_a$ (red histogram and red curve) is obtained from randomly sampling 10,000 times of the seismicity in a δt_a window (e.g., 2 hours) with uniformly distributed random starting time of the δt_a within 30 days before and after the *P*-wave arrival of the mainshock. Distribution-Λ (gray histogram and black curve) is obtained from randomly sampling 10,000 times of the seismicity in 60 days (δt_b) with uniformly distributed random starting time within half a year of the mainshock *P*-wave arrival (183 days before and after). In each panel, the black dashed line indicates the β_0 value, and the red dashed line shows the triggering threshold $\beta_{95\%}$. The identified triggering windows are outlined in red box panels (g and h). In such cases, distribution-$\mathcal{N}_a$ and distribution-Λ are clearly distinct from each other.

I *Compute β_0, the β-statistic of interest*. Following Equation 1, we compute the β-statistic of a time window (δt_a) after a posited triggering earthquake in a given region as β_0 with the expected event number as Λ. The event number is N_a for the time window δt_a and the background event number is N_b for the time window δt_b. The reference time period δt_b is 60 days , including 30 days before and 30 days after the *P*-wave arrival of a candidate triggering earthquake. The 60-day long δt_b time window provides a meaningful stable reference seismicity rate and including seismicity both before and after a candidate triggering earthquake poses a more strict requirement for claiming the elevated seismicity significant. We also compute β_b of an equal length time window immediately preceding δt_a with the same Λ, which defines the seismicity rate change prior to the time window of interest

II *Construct distribution-$\mathcal{N}_a$ to evaluate the significance of β_0*. We randomly resample (10,000 times) the seismicity in a δt_a window (e.g., 2 h) within δt_b. The starting time of the δt_a window tends to a continuous uniform distribution with the time range of δt_b as the support. With the sampled seismicity and the same expected seismicity (Λ), we obtain a set of 10,000 β-statistics. With the collection of β-statistics, we model the associated PDF with a kernel probability distribution, which sets the significance threshold of identifying a dynamic triggering case

III *Construct distribution-Λ to evaluate the background seismicity*. We randomly resample N_b (10,000 times) during time window δt_b (60 days) within half a year of the mainshock P-wave arrival. The starting time of the δt_b window tends to a continuous uniform distribution with the support as the time range of 183 days before and after the posited triggering earthquake (total sampling time range of 366 days). With the same β_0 and the set of 10,000 N_b, we then calculate a new collection of β-statistics, which is used to model the PDF of the distribution-Λ

IV *Evaluate triggering thresholds*. Finally, we assign a coverage probability ($\alpha \in [0, 1]$) and test for threshold exceedances based on the estimated distribution-$\mathcal{N}_a$ and distribution-Λ. If $\beta_0 \geq \beta_\alpha$, $\beta_0 \geq \beta^{\Lambda}_{(1-\alpha)}$, and

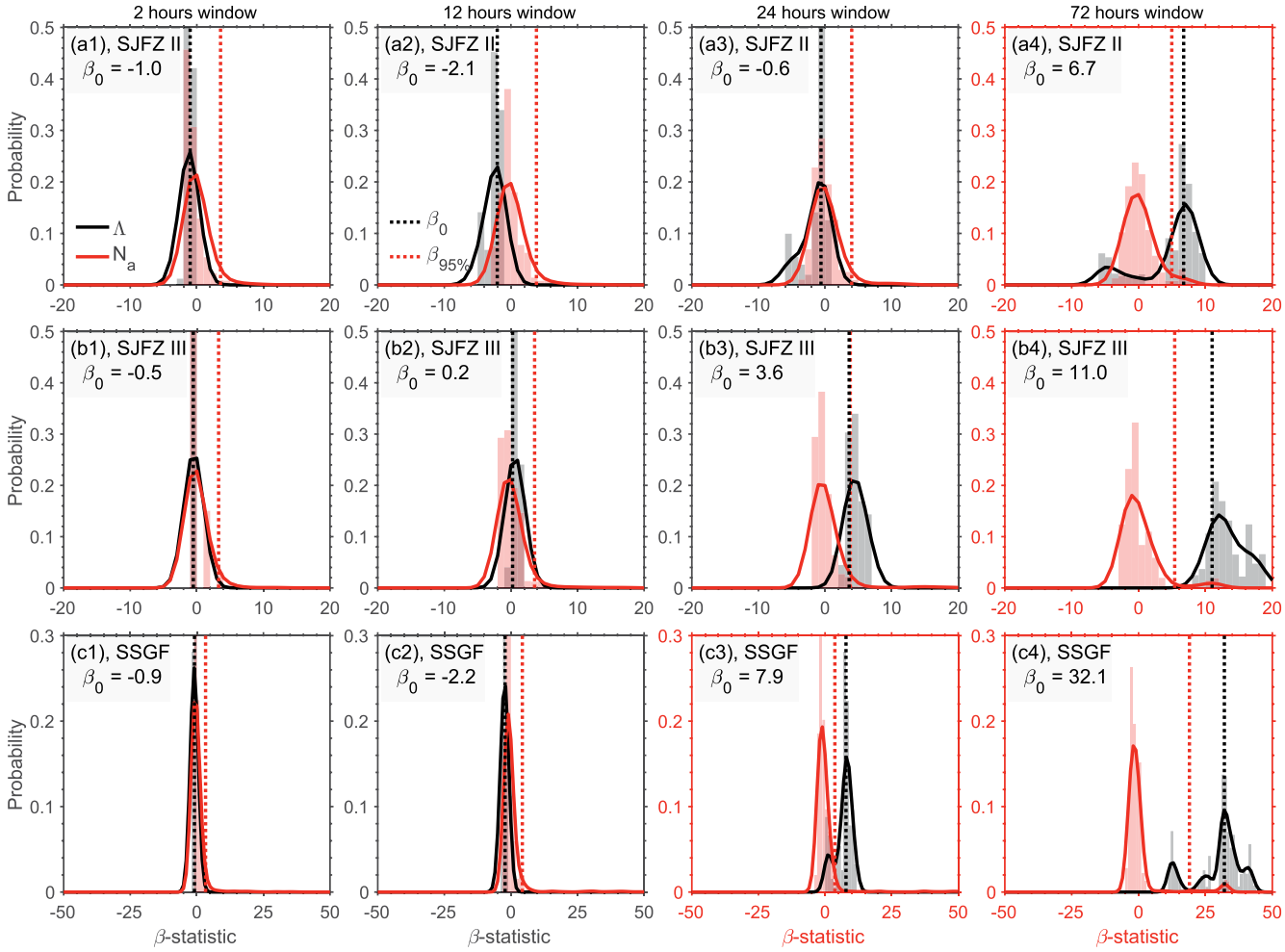

Figure 3. The β-statistic distributions in the SJFZ-II (a), III (b), and the SSGF (c) regions after the 2012 M_w 7.8 Haida Gwaii earthquake. The legends are similar to those in Figure 2. The rows show results of different regions, SJFZ-II (a), III (b), and the SSGF (c), and the columns show results of different time windows (2-, 12-, 24-, and 72-hours).

$\beta_0 \geq \beta_b$, we consider the candidate earthquake dynamically triggered seismicity during time window δt_a in the given region. We use the conventional $\alpha = 0.95$ (95%) confidence interval as a threshold value, denoted by $\beta_{95\%}$. The $\beta^{\Lambda}_{5\%}$ is thus the 5% confidence interval of the distribution-Λ. This threshold ($\beta^{\Lambda}_{5\%}$) can help to rule out the possibility that the identified significance was due to an abnormally low background seismicity rate. In other words, exceeding the $\beta^{\Lambda}_{5\%}$ threshold indicates that the background seismicity is typical or higher at a 95% confidence interval. The β_b offers a reference for seismicity rate change, which can help to exclude possible false identifications due to ongoing local seismic swarms rather than the passing seismic waves. If the seismicity rate has been significant before the seismic wave arrivals, the observed seismicity increase after the wave passage may not be solely due to the hypothesized dynamic triggering. We consider such cases as insignificant in this study. A more strict threshold (e.g., $\alpha = 0.99$) may also be desirable to rule out false positive detections

To illustrate the procedure, we take the 2012 M_w 7.8 Haida Gwaii earthquake as an example (Figures 2 and 3). To understand the seismicity rate change in region SJFZ-I that occurred two hours 2h after the passage of the seismic waves of the mainshock, we define the null hypothesis and an alternative hypothesis: (null) seismicity rates did not change during those two hours, and (alternative) the 2012 Haida Gwaii earthquake dynamically triggered local earthquakes in SJFZ-I during those two hours. Following our procedure, we first compute the β-statistic of interest of the time window, $\beta_0 = -0.8$. With the distribution-$\mathcal{N}_a$ and the

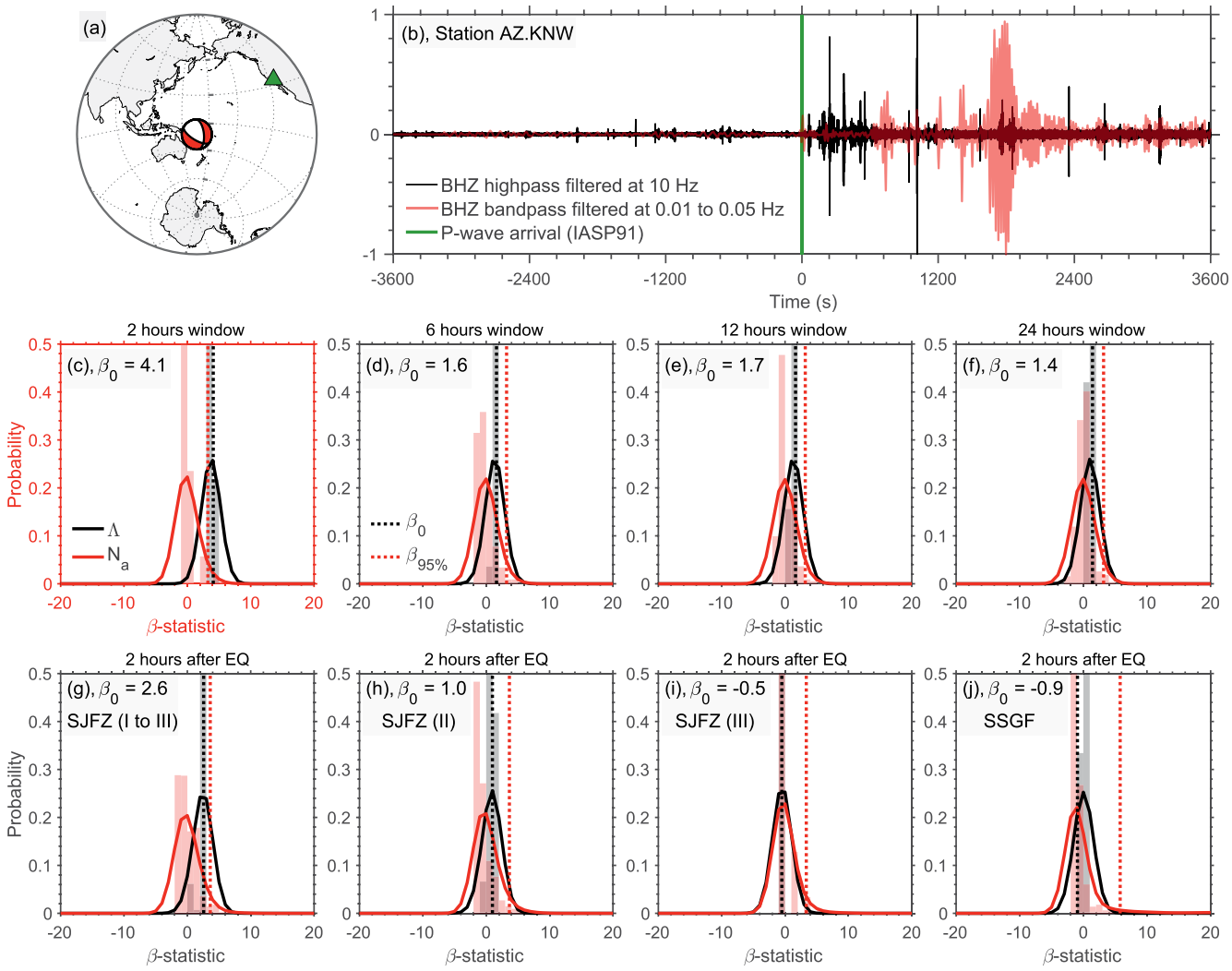

Figure 4. The 2012 M_w 6.0 Santa Cruz Islands earthquake (September 5, 2012) and the instantaneous dynamic triggering response in SJFZ-I. (a), location and the focal mechanism of the 2012 Santa Cruz Islands earthquake. (b), bandpass filtered seismogram of station KNW in Anza, California; the origin time (0) is the *P*-wave arrival time. (c–f), β-statistic distributions of the SJFZ-I region for four time windows. (g–j), β-statistic distributions of the other three fault systems for the 2 h time window. The legends are similar to those in Figure 2.

distribution-Λ, we obtain $\beta_{95\%} = 3.3$, $\beta^{\Lambda}_{5\%} = -3.2$, and $\beta_b = -0.8$. Thus the results cannot reject the null hypothesis (Figure 2e). In other words, with the detected seismicity, we have no evidence of dynamic triggering of earthquakes with $M \geq 0.3$ in SJFZ-I from this mainshock during these 2 h, and, if delayed triggering did occur, it must have been at least 2 h after the seismic wave passage. As we mentioned, using the 95% confidence interval as a threshold value ($\beta_0 \geq \beta_{95\%}$) is merely a subjective convention; it can and sometimes should be higher significance levels (Pankow & Kilb, 2020).

In this study, we consider changes in seismicity rate within 2 h of the passing seismic waves as instantaneous triggering ($\delta t_a = 2$ h), and changes seen in any other time windows are considered as delayed triggering ($\delta t_a = 6$, 12, or 24 h). If an earthquake caused both instantaneous and delayed triggering, we term the process as extended triggering, for which the dynamic triggering response was not only immediate but also continued after the passage of the mainshock seismic waves. The four window lengths are subjective choices and elevated seismicity duration can last for days for seismic swarms. It is more difficult to establish a causal connection between the passing waves and the change of seismicity for longer time windows based on our current physical understandings. Specifically, we do not investigate delayed triggering processes

beyond 24 h, but instead focus on the seismicity rate change during 6-, 12-, and 24-h time windows after the *P*-wave arrivals (Figures 2–4). This is because for long term delayed-dynamic triggering processes, it is often difficult to make a definitive case that the triggering was solely due to the transient dynamic wavefield (e.g., Brodsky, 2006; Lohman & McGuire, 2007; van der Elst et al., 2013). However, our method can be implemented to assess long term seismicity rate changes as well (Figures 2 and 3).

One important aspect of this method is how we represent the resampled statistics. The kernel probability distribution is a nonparametric representation of the probability density function of a random variable, which offers great flexibility and avoids assuming the distribution of the data (Bowman & Azzalini, 1997; Silverman, 1986). For example, a standard normal distribution PDF is a commonly used kernel. In this case, the kernel density estimator of the β-statistic is

$$\hat{f}_n(\beta) = \frac{1}{nh}\sum_{n}^{i=1} K\left(\frac{\beta - \beta_i}{h}\right) \tag{2}$$

where n is the sampling number, h is a smoothing parameter (bandwidth), and $K(x) = \frac{1}{\sqrt{2\pi}} e^{-\frac{1}{2}x^2}$ is the kernel. Effectively, the bandwidth h is a scaled standard deviation in this case. The bandwidth is a free parameter and can strongly influence the results. In theory, one would like to pick a small $h \to 0$ to capture the detailed data structure. However, noisy data can lead to biased distribution with a small h (Bowman & Azzalini, 1997). Here, we use $h = 1.5$ to smooth all the estimated distributions such that the $\beta_{95\%}$ threshold is conservatively large to robustly identify the dynamically triggered cases (Figures 2–4).

In summary, we use the distributions of the β-statistic to evaluate the significance of an elevated seismicity rate in a given region. This approach is data-driven and does not assume a probability density function of the β-statistic or the seismicity (e.g., we do not assume a Poisson distribution of the seismicity). This allows our method to accommodate the possibility of a temporally evolving background seismicity rate. More significantly, our method offers a rigorous and coherent framework to identify cases of both instantaneous (Figure 4) and delayed triggering (Figures 2 and 3).

When multiple triggering earthquakes are temporally close to each other, for example, separation time was shorter than the time window used to evaluate triggering, we consider that the identified dynamically triggered seismicity was due to both or all of the triggering events that occurred during the time window. We report the events as triggering earthquakes, but do not differentiate the triggering contributions of each earthquake separately.

3.2. Peak Ground Velocity and Normalized Velocity Spectra

We measure the peak ground velocity of the identified triggering earthquakes from broadband seismic stations that are located in the SJFZ and SSGF regions (Figures 1 and 5–7). The SJFZ-I region is the best-instrumented segment and there are no available broadband seismic stations in the SJFZ-III region (Figure 1). After the preprocessing procedure (Section 2.3), we first compute envelope functions of the 2-h three-component velocity seismograms that are filtered at 0.01–0.05 Hz and obtain an average envelope function for each station by computing the geometric mean of the three-component seismogram-envelopes. We then measure the maximum values of the geometric mean of the average envelopes for the fault segments respectively (Figure 5). Using the geometric mean can effectively suppress potential biases due to instrumental malfunctions. To test the hypothesis of a PGV triggering threshold, we also evaluate the PGV values of "twin" nontriggering earthquakes that are adjacent to the triggering earthquakes (Figure 5). We defined "twin" nontriggering earthquakes to be within 200 km and 0.25 moment magnitude (M_w) range of the triggering earthquakes during the same time period (2008–2017). The triggering and the "twin" nontriggering earthquakes share similar wave propagation paths, and any deviations in the measured PGV values at a given site may reflect differences in the source attributes. On average, the triggering and "twin" nontriggering earthquakes are 10,000 km away from the testing sites with the closest event 190 km away from Anza. We further compare these measured values with ground motions that are estimated from an empirical ground motion regression (Peña Castro et al., 2019; van Der Elst & Brodsky, 2010; Velasco et al., 2004):

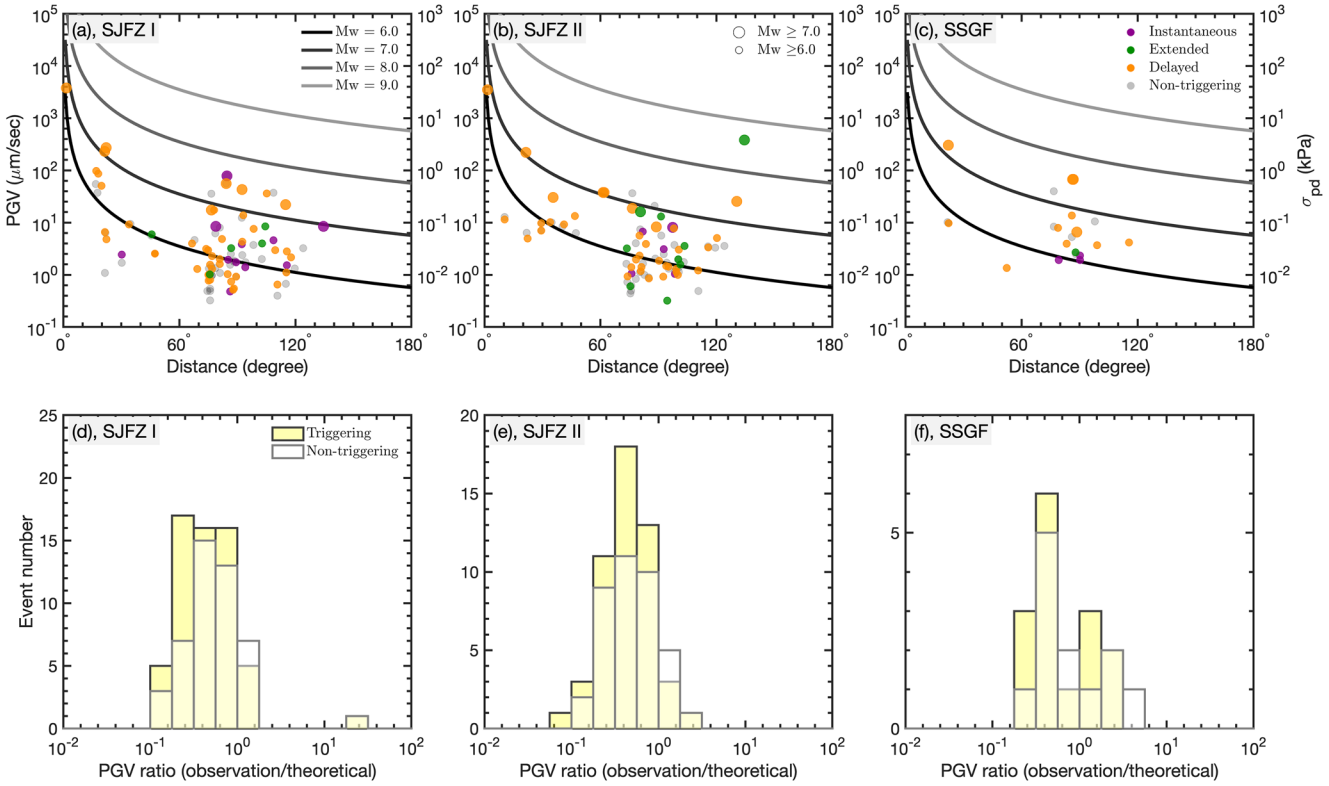

Figure 5. Peak ground velocity or peak dynamic stress σ_{pd} in SJFZ-I (a,d), II (b,e), and SSGF (c,f) from the triggering and nontriggering "twin" earthquakes. The PGVs are measured from three-component seismograms (a–c). The peak dynamic stress is inferred from the measured PGV value following $\sigma_{pd} = PGV \times \frac{G}{c}$ with G as 32 GPa and c as 3.5 km/s (Peña Castro et al., 2019). The top row shows the measured PGV values for the triggering earthquakes (color dots) and the "twin" nontriggering earthquakes (gray dots) and the estimated PGV curves as functions of epicentral distance (Equation 3). The bottom row shows the distributions of the measured-estimated PGV ratios of the three regions (d–f).

$$\mathrm{PGV} = \frac{2\pi A_{20}}{20} \tag{3}$$

where A_{20} is the 20 s period surface wave amplitude in microns, which is obtained from

$$\mathrm{M_s} = \log A_{20} + 1.66 \log \Delta + 2.0 \tag{4}$$

here, M_s is approximated with M_w (Hanks & Kanamori, 1979), and Δ is the epicentral distance (degrees) between the earthquake and a reference location in SJFZ (116.593°W, 33.537°N) (Figures 1 and 5).

Furthermore, we investigate the velocity spectra of the triggering and the "twin" nontriggering earthquakes (Figure 8). We compute the velocity spectra with unfiltered 1-h three-component seismograms after the *P*-wave arrivals and we also compute the noise spectra with records half an hour before the *P*-wave arrivals. The velocity spectra can help to identify possible triggering signatures in the frequency-dependent ground motions (Brodsky & Prejean, 2005; Guilhem et al., 2010; Kane et al., 2007). The spectra are computed with a multitaper power spectral estimation method (e.g., Barbour & Parker, 2014; Prieto et al., 2007) with discrete prolate spheroidal tapers and a time-bandwidth product of 6 to balance the spectral resolution. For each event, three-component velocity spectra of all stations are computed independently. After self-normalization, these spectra are averaged to obtain a geometric mean spectrum of the event. These event spectra are further geometrically averaged to isolate possible influences of the frequency content. For example, spectra of the triggering and the "twin" earthquakes are compared in Figure 8, and the velocity spectra of events that result instantaneous and/or delayed-dynamic triggering are compared for the regions that had sufficient instrumentation as well (Figure 8).

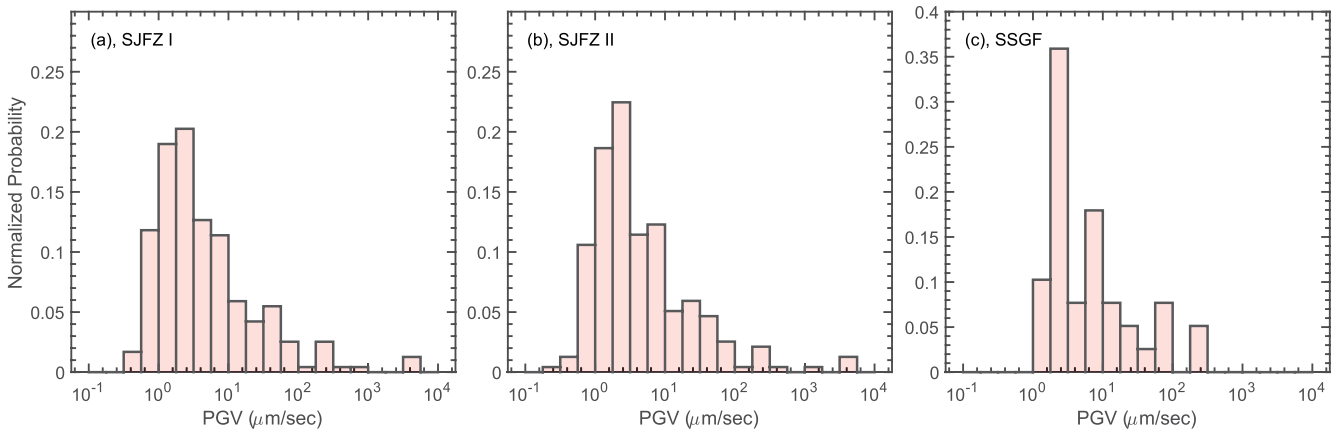

Figure 6. Measured peak ground velocity distributions of the triggering earthquakes. (a), SJFZ-I. (b), SJFZ-II. (c), SSGF.

3.3. Comparisons With Observed Dynamic Strain

As a further check on results from the ground velocity measurements, we measure the peak dynamic strain (PDS) values from borehole strainmeters located in the SJFZ-I and II regions (Figure 1). There are no borehole strainmeters in either the SJFZ-III or SSGF regions. From more than 2 decades of continuous strain records at the Piñon Flat Observatory and Durmid Hill, Agnew and Wyatt (2014) obtained a general description of peak strains as a function of moment magnitude and epicentral distance (here Δ is in kilometer):

$$\log \mathrm{PDS} = 0.95M_w - 1.65\log\Delta - 11.8 \tag{5}$$

This distance-dependent strain scaling relationship shares similarities with the surface wave amplitude-distance relationship of Equation 4 (Agnew & Wyatt, 2014). It shows that strain and velocity in the direction of propagation are theoretically proportional for a perfectly polarized plane wave (e.g., the radial extension and radial velocity). In this study, we directly measure PDS values of both the triggering earthquakes and the "twin" nontriggering earthquakes and compare the observations with the empirically estimated PDS values computed from Equation 5 (Figure 9).

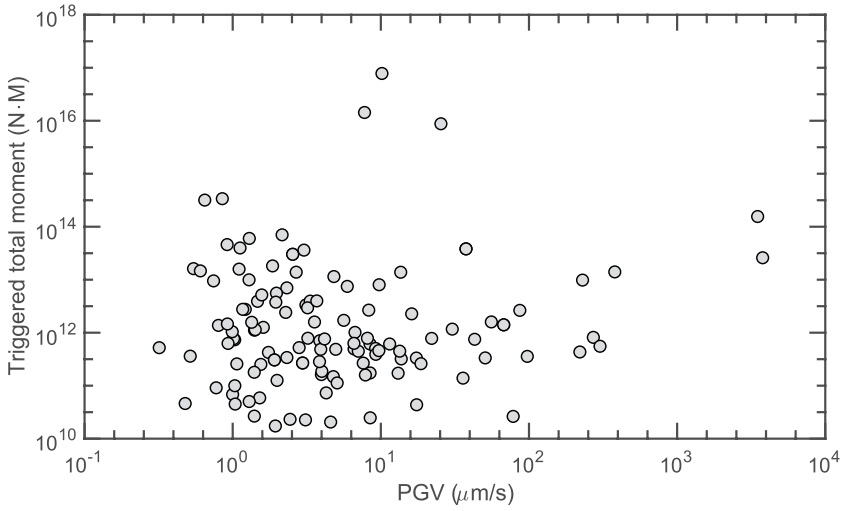

Figure 7. Measured peak ground velocity and the triggered total moment.

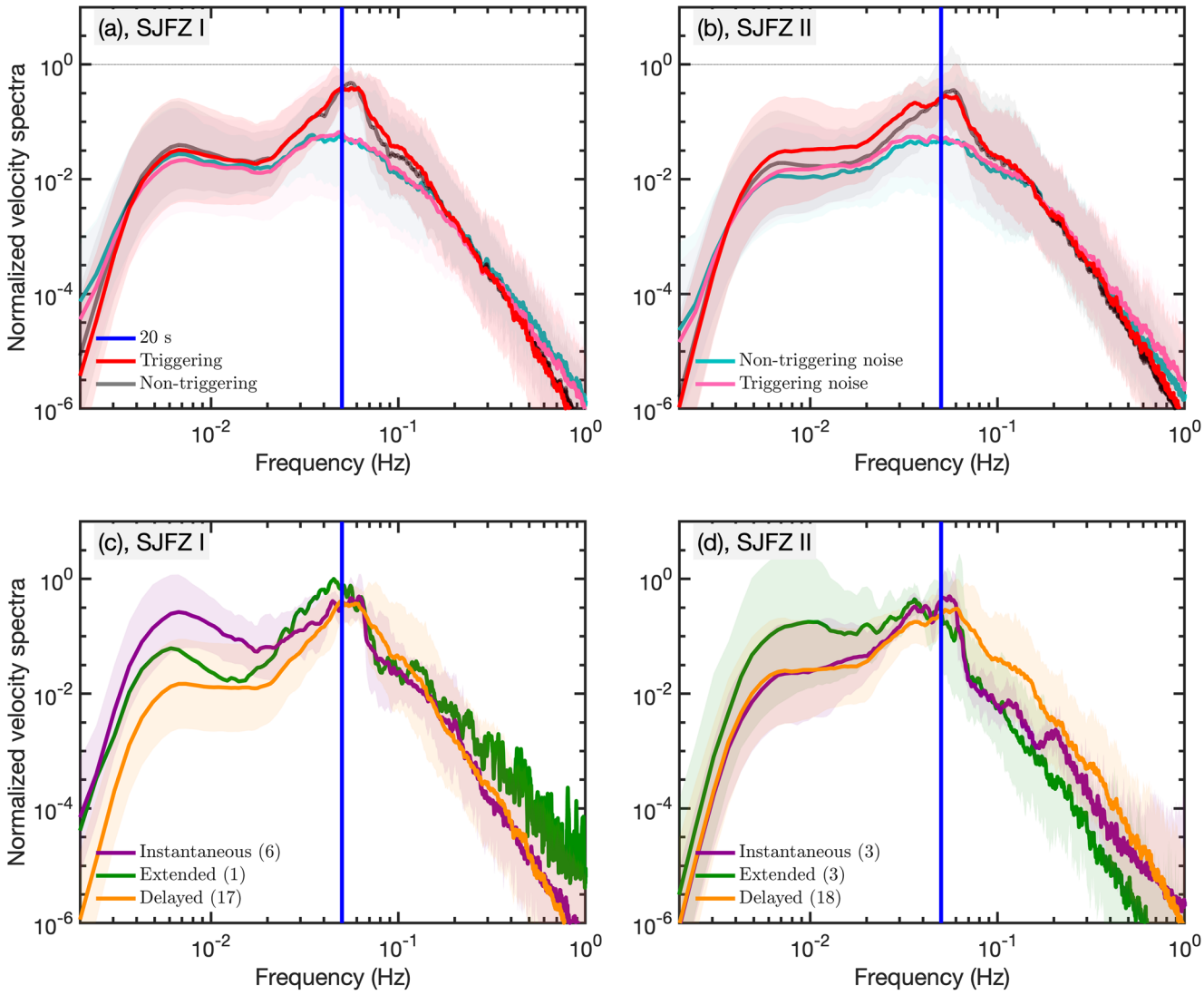

Figure 8. Geometrically averaged normalized velocity spectra in SJFZ-I (a,c) and II (b,d) of the triggering and nontriggering earthquakes. The shaded patches show the range of the spectra values (within one standard deviation). The top row shows the mean spectra of the triggering and nontriggering earthquakes (a,b). The bottom row shows the spectra of the instantaneous-, extended-, and delayed-dynamic triggering cases. Numbers of the triggering earthquakes are shown in the parentheses (c,d).

4. Results

We find evidence of frequent dynamic triggering of microearthquakes in Southern California from globally distributed $M_w \geq 6$ earthquakes (Figure 10). On average, more than 1 out of every 5 $M_w \geq 6$ earthquakes from 2008 to 2017 (274 triggering earthquakes) have caused significant increases in seismicity on at least one of the fault segments (SJFZ-I to III and SSFZ) during one of the four time windows (2, 6, 12, and 24 h). There is no clear correlation between the earthquake magnitude and the triggering rate. The results show that moderate magnitude earthquakes have similar potentials to dynamically trigger microearthquakes in Southern California, and local earthquake triggerbility should not be evaluated solely based on the posited earthquake magnitude. Earthquakes with $M_w \geq 8$ occur too infrequently to obtain a reliable triggering rate.

We observe that earthquakes from back-azimuthal directions of 60°–90° and 180°–210° are more likely to trigger earthquakes in Southern California (Figure 10). Because of the uneven global earthquake distribution, we evaluate the triggering earthquake percentage instead of the number of triggering earth-

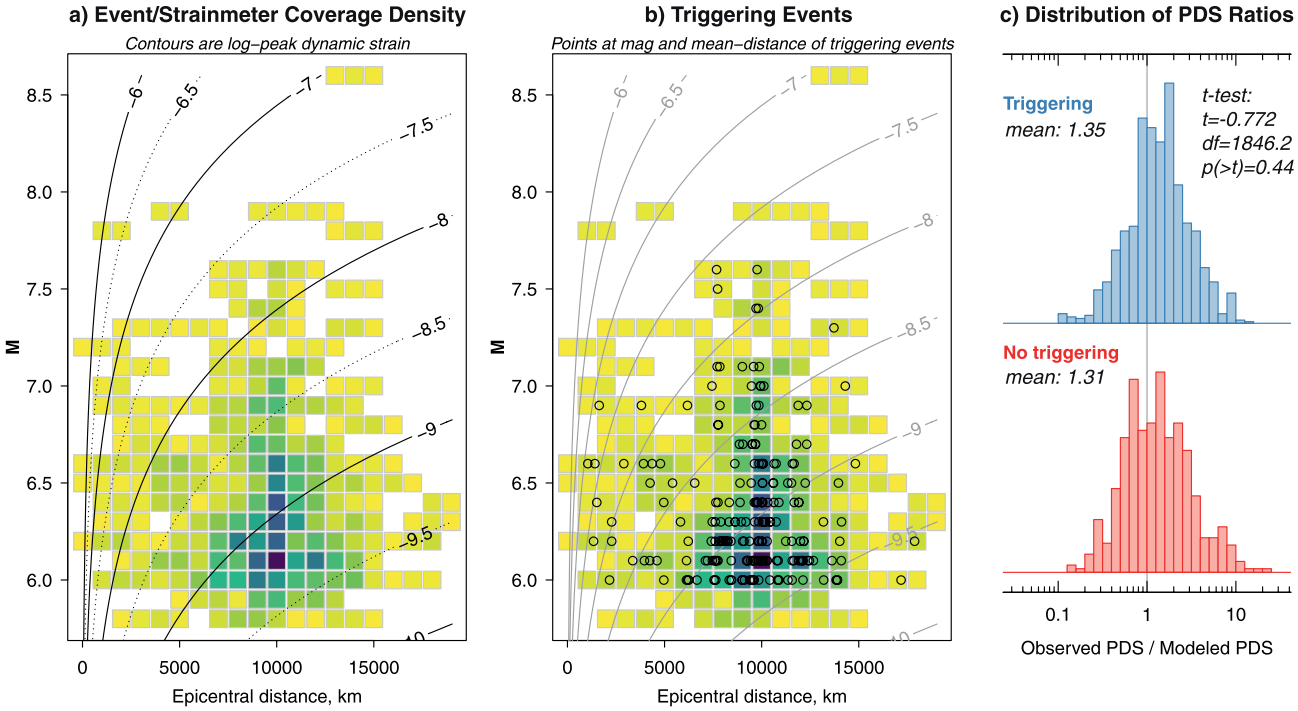

Figure 9. Peak dynamic strains (PDS) for the SJFZ I and II regions. (a), Event-to-strainmeter data coverage by moment magnitude and epicentral distance (km); darker colors represent higher density of data coverage. Contours are log-PDS according to the scaling relationships in Agnew and Wyatt (2014); the stations we used are shown in Figure 1. (b), Same figure as (a) but with circles showing source-receiver pairs where the event is a triggering event. (c), The distributions of the log-ratio of observed-to-estimated PDS (e.g., the contours in (a)). There are two distributions plotted on the same density scale, one for triggering events and the other for "twin" nontriggering events. On average the ratios for triggering events are marginally higher than for nontriggering events, but the results of a Student's *t*-test for the given degrees of freedom (df) indicate that this mean difference is insignificant. We also note the heavier upper tail of the PDS ratios associated with no triggering.

quakes from different directions. We divide the back azimuth into 30° azimuthal bins and the triggering percentage is computed as the ratio between numbers of the triggering earthquake and the candidate earthquake in each bin. For each fault segment, the triggering rate is below 10% for earthquakes with different magnitudes or at different directions. This shows that one triggering earthquake rarely triggers seismicity at multiple fault segments, and the triggering response is independent for the fault segments.

We observe a range of dynamic triggering responses in the SJFZ and SSGF regions (Figures 2–4, Tables 1 and 2). For example, although no earthquakes were instantaneously triggered by the 2012 M_w 7.8 Haida Gwaii earthquake in either the entire SJFZ or SSGF regions (Figures 2 and 3), the SJFZ-I and SSGF regions show evidence of delayed triggering in the 24-h window following the passage of seismic waves (Figures 2 and 3). In contrast, there is no strong evidence indicating dynamical triggering in SJFZ-II or SSGF-III during that time window or in shorter time windows (Figure 3). Interestingly, seismicity rates are significantly elevated in the 72-h period following the Haida Gwaii earthquake in all four regions. For the SSGF section, the β-statistic of the 3-day time window is 32.1, nearly three times that of anywhere in the SFJZ, which suggests an energetic delayed triggering process (Table 1). Another example of varying response is the 2012 M_w 6.0 Santa Cruz Islands earthquake (September 5, 2012), which instantaneously triggered earthquakes in SJFZ-I, but did not cause any clear increase of seismicity in the other three regions (Figure 4). These observations show spatial and temporal variations of the dynamic triggering responses at the four fault subsystems.

The susceptibility to dynamic triggering also varies, with the total number of triggering earthquakes being different for each fault segment (Figures 11 and 12) . The SSGF region appears to be most susceptible to dynamic triggering with a total triggering rate of 7.7% (100 triggering earthquakes, Figure 12d) compareing to 4.9% (64 earthquakes) at SJFZ-II. The distribution of triggering window lengths varies from

Table 1
β-statistics of the 2012 M_w 7.8 Haida Gwaii Earthquake

β-statistic	SJFZ-I	SJFZ-II	SJFZ-III	SSGF
β_0 (2-h)	−0.8	−1.0	−0.5	−0.9
$\beta_{95\%}$ (2-h)	3.3	3.6	3.3	3.3
$\beta^{\Lambda}_{5\%}$ (2-h)	−3.2	−3.7	−2.9	−3.5
β_0 (6-h)	2.5	−1.2	−0.9	−1.5
$\beta_{95\%}$ (6-h)	3.6	3.7	3.3	3.9
$\beta^{\Lambda}_{5\%}$ (6-h)	0.1	−4.3	−3.3	−4.3
β_0 (12-h)	2.5	−2.1	0.2	−2.2
$\beta_{95\%}$ (12-h)	3.6	3.8	3.6	4.3
$\beta^{\Lambda}_{5\%}$ (12-h)	0.0	−5.5	−1.9	−5.1
β_0 (24-h)	5.1	−0.6	3.6	7.9
$\beta_{95\%}$ (24-h)	3.8	4.0	3.8	3.7
$\beta^{\Lambda}_{5\%}$ (24-h)	2.2	−5.8	1.6	0.4
β_0 (72-h)	8.8	6.7	11.0	32.1
$\beta_{95\%}$ (72-h)	4.7	5.0	5.4	19.0
$\beta^{\Lambda}_{5\%}$ (72-h)	4.3	−5.4	8.9	11.9

Table 2
β-statistics of the 2012 M_w 6.0 Santa Cruz Island Earthquake (September 5, 2012)

β-statistic	SJFZ-I	SJFZ-II	SJFZ-III	SSGF
β_0 (2-h)	4.1	1.0	−0.5	−0.9
$\beta_{95\%}$ (2-h)	3.2	3.7	3.4	5.8
$\beta^{\Lambda}_{5\%}$ (2-h)	1.2	−1.7	−2.9	−2.6
β_0 (6-h)	1.6	1.1	0.3	−2.0
$\beta_{95\%}$ (6-h)	3.2	3.8	3.7	10.7
$\beta^{\Lambda}_{5\%}$ (6-h)	−1.1	−1.8	−2.1	−3.3
β_0 (12-h)	1.7	0.8	−0.4	−2.5
$\beta_{95\%}$ (12-h)	3.2	4.0	4.2	17.3
$\beta^{\Lambda}_{5\%}$ (12-h)	−1.2	−2.4	−2.8	−3.5
β_0 (24-h)	1.4	1.1	−0.6	−4.1
$\beta_{95\%}$ (24-h)	3.2	4.2	5.1	22.0
$\beta^{\Lambda}_{5\%}$ (24-h)	−1.5	−2.7	−2.9	−5.0

fault to fault as well, showing different temporal evolution processes of the triggered seismicity. Intriguingly, the delayed-dynamic triggering cases ($6 \le \delta t_a \le 24$ h) are the most commonly observed modes at all four fault segments, while the near-instantaneously ($\delta t_a = 2$ h) dynamically triggered seismicity is observed for less than 25% of the triggering cases (Figure 12). The triggering variability is also reflected in the triggered earthquake number, which fluctuates on a case-by-case basis, and the minimum triggered numbers of earthquakes are 2, 3, 5, and 6 for the 2-, 6-, 12-, and 24-h time windows (Figure 11).

In addition to the diverse triggering responses, the triggered frequency (recurrence time) at each fault differs as well (Figure 12). Here, we take the intertriggering earthquake separation time as an approximate to infer how frequently does dynamic triggering occur at each subregion. We model the probability distribution of the intertriggering earthquake separation time with the generalized extreme value (GEV) distribution to understand the triggered frequency characteristics of each fault segment (Fan & Shearer, 2017; McFadden, 1978). The fitted GEV distributions are data-driven and can help to identify the smallest or largest values of a random variable with the PDF ($\rho(x)$) as:

$$\rho(x) = \frac{1}{\sigma} t(x)^{\kappa+1} e^{-t(x)} \tag{6}$$

where x is the separation time as the support for the GEV distribution, $t(x) = e^{-(x-\mu)/\sigma}$ when $\kappa = 0$, or $t(x) = \left(1 + \kappa \frac{(x-\mu)}{\sigma}\right)^{-1/\kappa}$ when $\kappa \neq 0$, and μ, σ, and κ are the location, scale, and shape parameters (Figure 12). In fitting the GEV to triggered frequency in the SJFZ-I and the SJFZ-III fault segments, we find that dynamically triggered events are most likely seen every ~73 days, whereas the frequencies of the SJFZ-II and the SSGF regions likely exceed 100 days (Figure 12). For all the candidate earthquakes, the peak occurrence frequency is less than one day.

Peak ground velocity is a commonly explored triggering threshold for earthquake dynamic triggering processes (e.g., Gonzalez-Huizar & Velasco, 2011; Peña Castro et al., 2019; van Der Elst & Brodsky, 2010). PGV generally associates with the transient peak dynamic stress (or strain) due to the passing seismic waves, assuming they are strongly polarized. Intuitively, dynamic triggering can be explained as a result of frictional failure because of a transient stress perturbation (Hill, 2008; Kilb, 2003). There were no broadband seismic stations in the SJFZ III area, therefore we only investigate PGV values in the SJFZ-I, II, and the SSGF areas. The observed PGV values of the triggering and "twin" nontriggering earthquakes cluster together, and we do not observe a clear difference in the PGV amplitudes between the two groups (Figures 5a–5c). To further investigate similarities and differences between triggering and "twin" nontriggering earthquakes, we normalize the measurements with empirical estimations obtained from Equation 3. We observe that the PGV ratio patterns of the triggering and "twin" nontriggering earthquakes are statistically indistinguishable (Figures 5d–5f), suggesting no apparent systematic differences among these earthquakes. However, we find the measured PGVs are systematically lower than the estimated ones (Figures 5d–5f). This is likely because we geometrically averaged the envelopes from records within each fault segment. Furthermore, local site effects and source radiation patterns can strongly influence the PGV

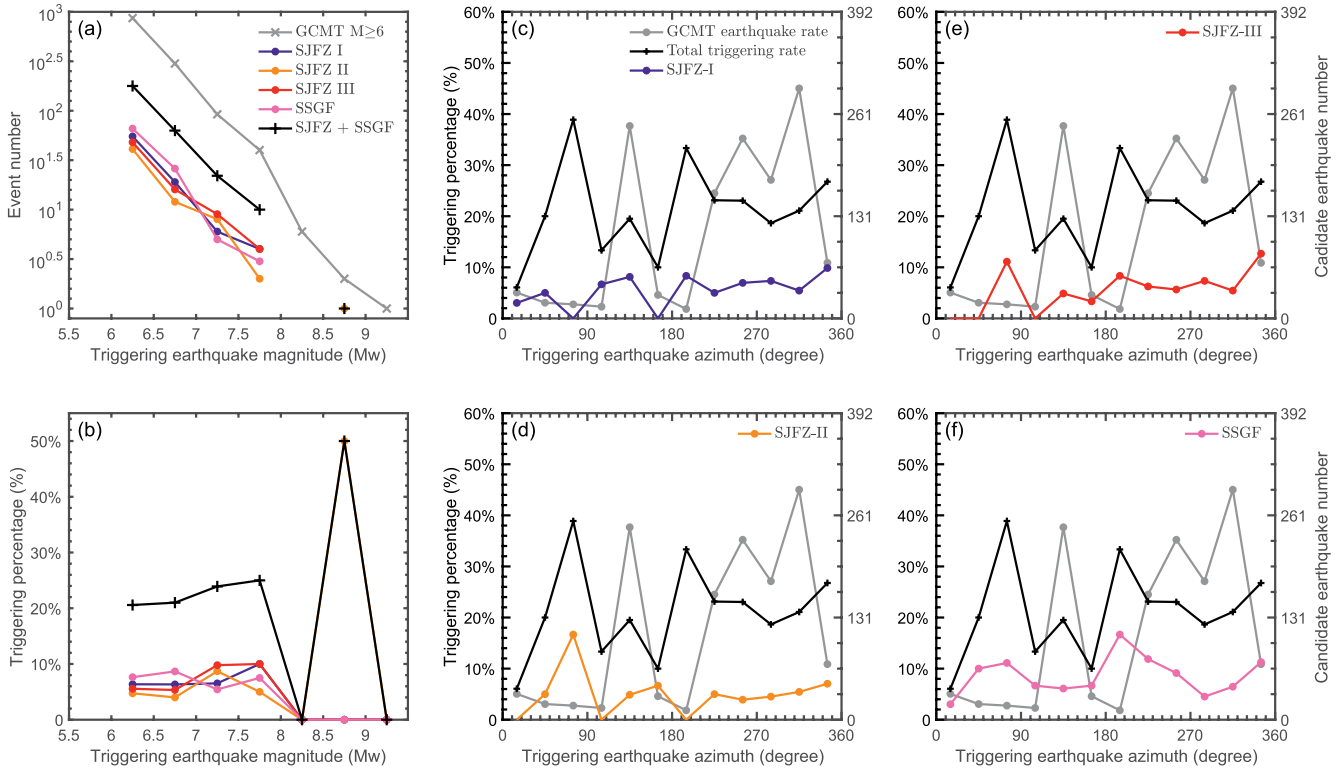

Figure 10. Dynamic triggering percentages in the SJFZ and SSGF regions. (a), Triggering number of events with 0.5 magnitude (M_w) bins. (b), Triggering percentage with 0.5 magnitude (M_w) bins. (a) and (b) share the same legends. (c–f), Triggering percentage of earthquakes in 30° azimuthal bins. The gray line shows the azimuthal distribution of the candidate earthquakes. The black line shows the total triggering percentage for the SJFZ and SSGF regions. The colored lines show triggering percentages of each subregion.

measurements and our current set of observations are insufficient to isolate the origins of the deviation between the measurements and the empirical estimations (Figure 5).

The absolute PGV values of the triggering earthquakes span five orders of magnitude from 0.1 to 10^4 μm/s with 1–10 μm/s as the most probable range for the study regions (Figure 6). To further explore the PGV impacts on the triggering response, we examine the relationship between the PGV values and the triggered moment of local earthquakes (Figure 7). We consider all the microearthquakes during the triggering time windows in a given subregion as triggered earthquakes. Assuming the local magnitudes equal to the moment magnitudes, we calculate the triggered total moment as the sum of the triggered earthquake moments. We find that the strength of the response (triggered total moment) does not seem to correlate with the peak ground velocity and the triggered total moment mostly ranges from 10^{10} to 10^{14} N·M, corresponding to an earthquake magnitude from 0.6 to 3.3 (Figure 7).

The peak dynamic strain (PDS) results (Figure 9) are in agreement with the PGV results for the SJFZ-I and II sections. The magnitude-distance distribution of the triggering events reflects the data coverage (Figure 9b), and there is no statistically significant difference in mean ratios of the observed and estimated PDS values between the triggering and nontriggering events (Figure 9c). Furthermore, we confirmed that there are no systematic trends in the PDS ratios as a function of either moment magnitude or event-to-station distance.

The amplitude of low-frequency ground motion (e.g., at 20 s periods and longer) has been proposed as a key attribute for nucleating earthquakes via dynamic triggering (Brodsky & Prejean, 2005; Guilhem et al., 2010). In this study, on average, there are relatively minor differences in the normalized velocity spectra between triggering and nontriggering events (Figures 8a and 8b). However, at both the SJFZ-I and SJFZ-II regions, the relative low-frequency ground motions of instantaneous-, delayed-, and extended-triggering processes diverge from each other, showing different velocity spectra. The divergence is particularly clear for ground

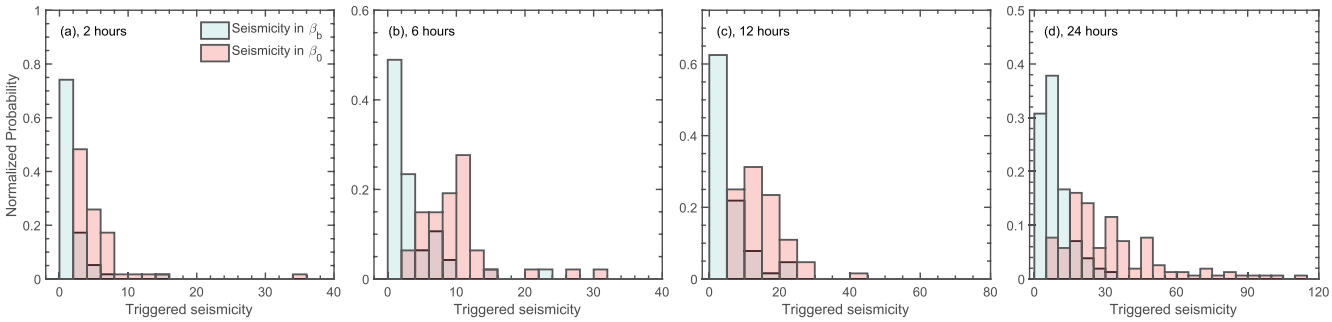

Figure 11. Dynamic triggering responses (number of earthquakes) of different time windows (2-, 6-, 12-, 24-h). The red histogram shows the triggered earthquake numbers (N_a), which were used for β_0 calculations. The blue histogram shows the earthquake numbers in the preceding time windows, which were used for β_b calculations. For the 2- (a), 6- (b), 12- (c), and 24-h (d) windows, the N_a values range from 2–34, 3–89, 5–140, and 6–1,220, respectively.

motions in SJFZ-I, although the pattern is not consistent between SJFZ-I and SJFZ-II (Figures 8c and 8d). There are no records in SJFZ-III or not enough records in SSGF for a similar spectral analysis.

5. Discussion

5.1. Triggering by Intermediate and Deep Earthquakes

Crustal as well as intermediate and deep earthquakes are susceptible to dynamic triggering (Fan et al., 2019; Freed, 2005; Myers et al., 1995; Tibi et al., 2003), but the triggering processes of earthquakes at different depths are often evaluated separately. Examples of this include shallow seismicity dynamically triggered by crustal earthquakes and remote triggering of intermediate and deep earthquakes due to events at similar depths (Cai & Wiens, 2016; Luo & Wiens, 2020; Hill & Prejean, 2015). In particular, cases of intermediate and deep earthquakes dynamically triggering crustal seismicity are rarely reported, and the absence of such cases is not considered unusual because of the low surface-wave amplitudes associated with these earthquakes.

Our observations show that intermediate and deep earthquakes commonly dynamically trigger earthquakes in the SJFZ and SSGF regions, and the overall triggering responses of these earthquakes are statistically comparable to those of shallow earthquakes (Figures 2, 10, and 13). Of the 1,306 candidate triggering earthquakes tested in this study, 250 events are intermediate and deep earthquakes ($M_w \geq 6.0$, depth ≥ 100 km). Of these 250 events, we find that 47 of them dynamically triggered seismicity in the SJFZ or SSGF regions during the study period, including 8 $M_w \geq 7.0$ triggering earthquakes (e.g., Figure 13); this represents an average triggering rate of ~19%. Some notable examples include the 2008 M_w 7.3 Sea of Okhotsk earthquake (depth 502.3 km), the 2011 M_w 7.0 Vanuatu Islands earthquake (depth 151.6 km), and the 2015 Peru deep earthquake doublet (M_w 7.5 and M_w 7.6 at depth of 610.7 km, occurred within 10 min of each other) (Figure 13). These observations suggest that dynamic triggering responses in Southern California likely correlate with attributes of the local ground motions, rather than specific source properties of the triggering earthquakes.

5.2. Remote Dynamic Triggering Rates

During the study period, we observe ~1 out of 5 $M_w \geq 6.0$ earthquakes dynamically triggered microearthquakes in at least one of the four tested areas of Southern California. This rate is comparable to the ~30% triggering rate of large aftershocks ($M \geq 5$) due to the near-to-intermediate field dynamic triggering of $M7$ earthquakes (Fan & Shearer, 2016). However, our observed triggering rates, including the triggering rate of $M_w \geq 7.0$ (25%), are considerably lower than the triggering rate reported in Velasco et al. (2008) (75%), which found that 12 out of 15 $M \geq 7.0$ earthquakes have caused near instantaneously dynamically triggered earthquakes. The ubiquitous phenomenon of dynamic triggering in Velasco et al. (2008) was observed from investigating 500 globally distributed stations, while our observation was drawn from seismicity rate changes in Southern California. Presumably, in the Velasco et al. (2008) study, multiple critically stressed fault systems may have been dynamically triggered by the passing waves but may not have been simultaneously

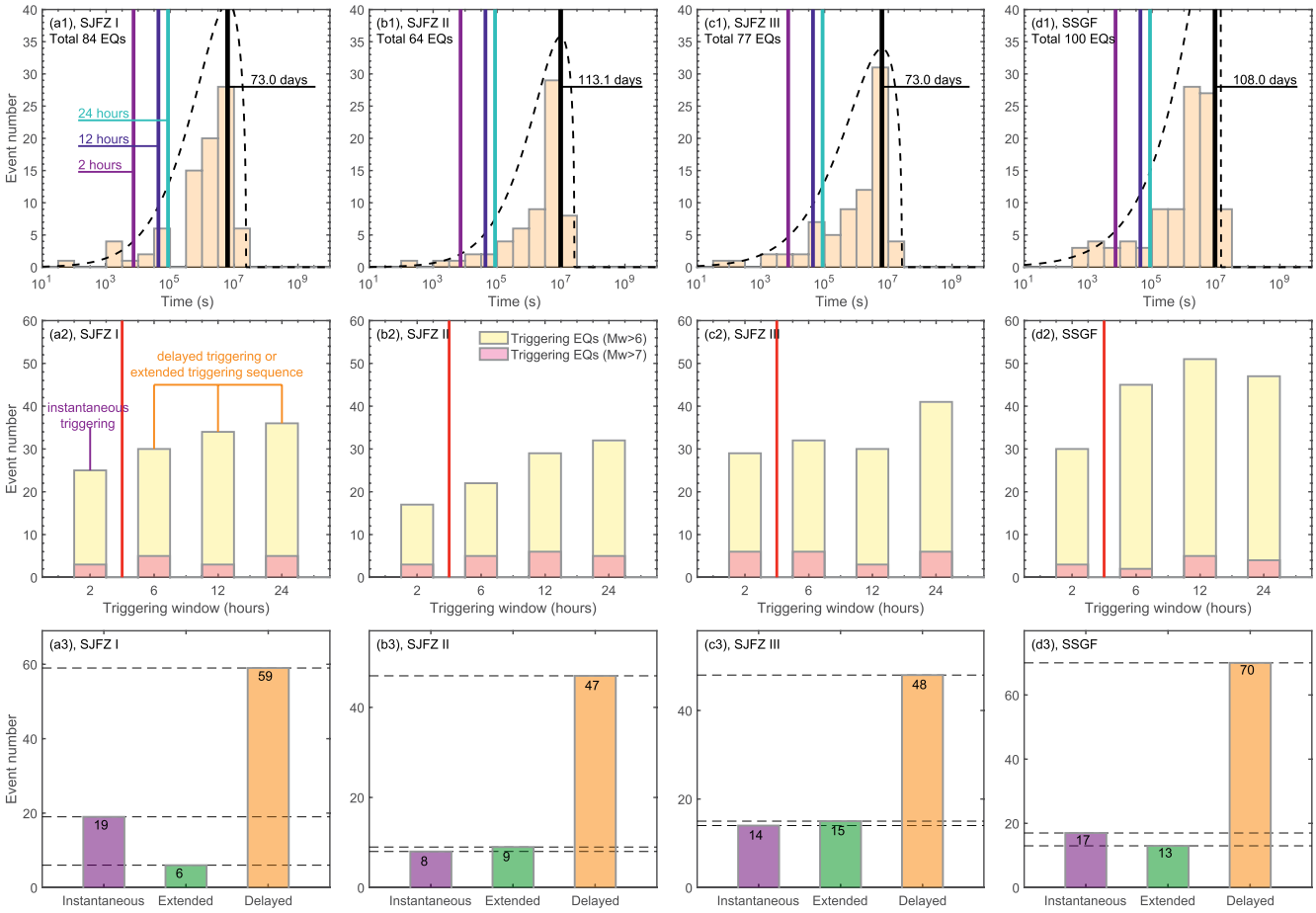

Figure 12. Dynamic triggering characteristics of the SJFZ (a-c) and SSGF (d) regions. The columns show results of different regions. The top row shows the intertriggering earthquake separation time distributions, the fitted generalized extreme value (GEV) distributions are shown as the black dash curves. The shape parameter (κ), scale parameter (σ), and location parameter (μ) are $10^{-0.7290}/10^{1.0833}/10^{5.8908}$, $10^{-0.7652}/10^{0.9904}/10^{6.1202}$, $10^{-0.7334}/10^{1.2059}/10^{5.7792}$, and $10^{-0.8910}/10^{1.1651}/10^{5.8452}$ for the SJFZ-I , II, III, and SSGF regions, respectively. The middle row shows the triggering earthquake number distributions with respect to the four time windows (2-, 6-, 12-, 24-h). The bottom row shows the triggering mode distributions (instantaneous-, extended-, and delayed-dynamic triggering).

triggered, which out-of-phase responses may lead to a larger overall triggering rate. The reported ubiquitous triggering pattern in Velasco et al. (2008) does not exclude a relatively low triggering rate on an individual fault system. For example, we also observe that the four regions individually have lower triggering rates comparing to the overall average triggering rate when considering all four sections at once (Figure 10). These observations show that the dynamic triggering responses vary spatiotemporally, and that small scale fault structures or stress states may be the predominant factors modulating the triggering responses, which respond in turn to a wide range of seismic wavefield amplitudes (van Der Elst & Brodsky, 2010). If this holds true, the absence of remote triggering cases in regions without anthropogenic stress perturbations (e.g., van der Elst et al., 2013) would indicate that local structures and stress regimes may be prohibitive of dynamic triggering (e.g., Harrington & Brodsky, 2006).

Intriguingly, our observed triggering rate (over 20%) is significantly larger than the triggering rate documented in Pankow and Kilb (2020), which also examined the possible triggering cases in Anza, California (SJFZ-I). They found that remote dynamic triggering is rare (<2%) by examining 500 triggering earthquakes and four 33-year-long earthquake catalogs in the Western US. One possible explanation for the higher triggering rate in this study is the magnitude of completeness (M_c) of the QTM catalog. The nominal M_c of the QTM catalog is 0.3, which is almost one magnitude smaller than the M_c of the catalogs analyzed in Pankow and Kilb (2020). For example, our statistical procedure would suggest that the 2012 Haida Gwaii earthquake did not dynamically trigger microearthquakes in Southern California within 24 h of its occurrence, when only using earth-

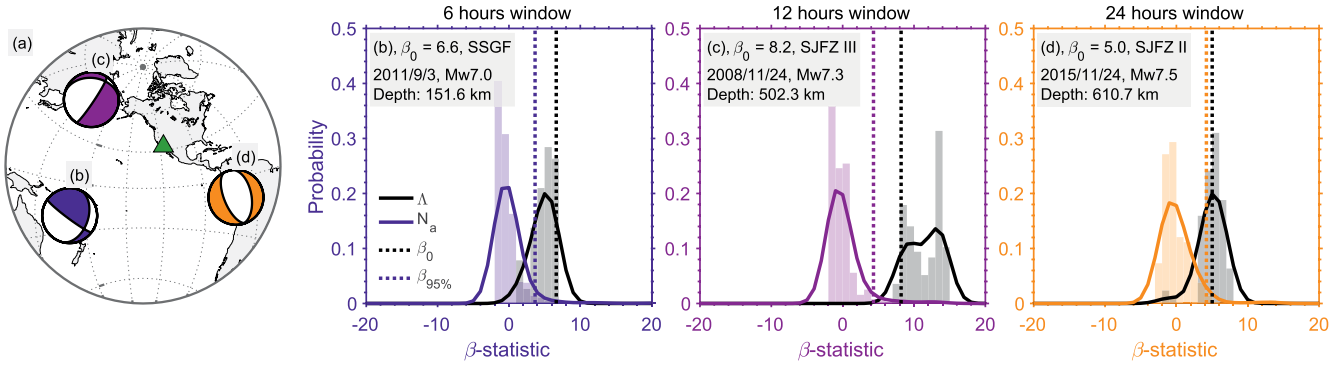

Figure 13. Dynamic triggering cases in SJFZ and SSGF caused by three example intermediate and deep $M_w \geq 7.0$ earthquakes. (a), Locations and the focal mechanisms of the example intermediate and deep earthquakes. (b), Dynamic triggering response at the SSGF region due to the 2011 M_w 7.0 Vanuatu Islands intermediate depth earthquake. (c), Dynamic triggering response at the SJFZ-III region due to the 2008 M_w 7.3 Sea of Okhotsk deep focus earthquake. (d) Dynamic triggering response at the SJFZ-II region due to the 2015 M_w 7.5 and M_w 7.6 Peru deep earthquake doublet.

quakes with $M \geq 1.3$ for a similar analysis (Figure 14). Within three days (72 h), only the SSGF region shows a statistically significant seismicity elevation (Figure 14). This also implies that we may have missed some dynamically triggered earthquakes with magnitudes smaller than 0.3. In addition, different procedures used to identify statistically significant triggering may also lead to discrepancies, including background seismicity rate choices and fault area segmentations (Marsan & Nalbant, 2005). Future studies implementing the same procedures to comparatively investigate the triggering cases may help to understand this apparent inconsistency.

5.3. Spatiotemporally Evolving Triggering Threshold ($\beta_{95\%}$)

As noted by previous studies, using $\beta_0 \geq 2.0$ as a threshold to identify dynamic triggering is insufficient to robustly characterize a significant increase in seismicity: the β-threshold varies with different triggering earthquakes or with different receiver faults (e.g., Marsan & Nalbant, 2005; Cattania et al., 2017; Prejean & Hill, 2018; Pankow & Kilb, 2020). We find no evidence to the contrary; there is a similar pattern of clear spatial and temporal variations of the triggering threshold, $\beta_{95\%}$ (Figure 15). Spatially, the triggering threshold ($\beta_{95\%}$) shows different features at each fault system even though the SJFZ segments are adjacent to each other. In general, the $\beta_{95\%}$ is greater than 2.0 with extreme cases as large as ~23 for the SSGF region. The spatial differences likely associate with variable rates of background seismic activity between the regions, which likely reflect the local stress state and material strengths. For example, the larger $\beta_{95\%}$ of the SSGF region may be due to frequent energetic earthquake swarms, which may have been influenced by geothermal production activities (e.g., Cheng & Chen, 2018; Crandall-Bear et al., 2018).

For the same fault segment, we observe a range of $\beta_{95\%}$, reflective of the temporal evolution of local seismicity. For example, in SSGF, there is a wide range of $\beta_{95\%}$, while the $\beta_{95\%}$ range is relatively small in SJFZ-III. Similarly, the β_0 has a large range of values indicating diverse triggering responses (Figure 15). These distinct triggering responses suggest that the local fault systems evolve differently and, possibly, multiple physical mechanisms modulate triggering processes.

5.4. Possible Physical Processes of Earthquake Dynamic Triggering

Multiple physical mechanisms have been proposed to explain earthquake dynamic triggering (Brodsky & Prejean, 2005; Freed, 2005; Hill & Prejean, 2015). The mechanisms can roughly be categorized as linear and nonlinear triggering processes. The linear triggering model, for example, Coulomb failure, directly correlates with the peak dynamic strain and explains dynamic triggering as a frictional failure due to transient stress perturbations incrementally exceeding the cohesive strength of the fault (Gonzalez-Huizar & Velasco, 2011; Hill, 2008; Kilb, 2003). Such linear models suggest that the triggered seismicity results from a "clock-advance" effect: faults are critically stressed and ready to rupture, and the dynamic stress increment from the seismic waves simply advances the cycle of regular earthquakes. This mechanism can intuitively

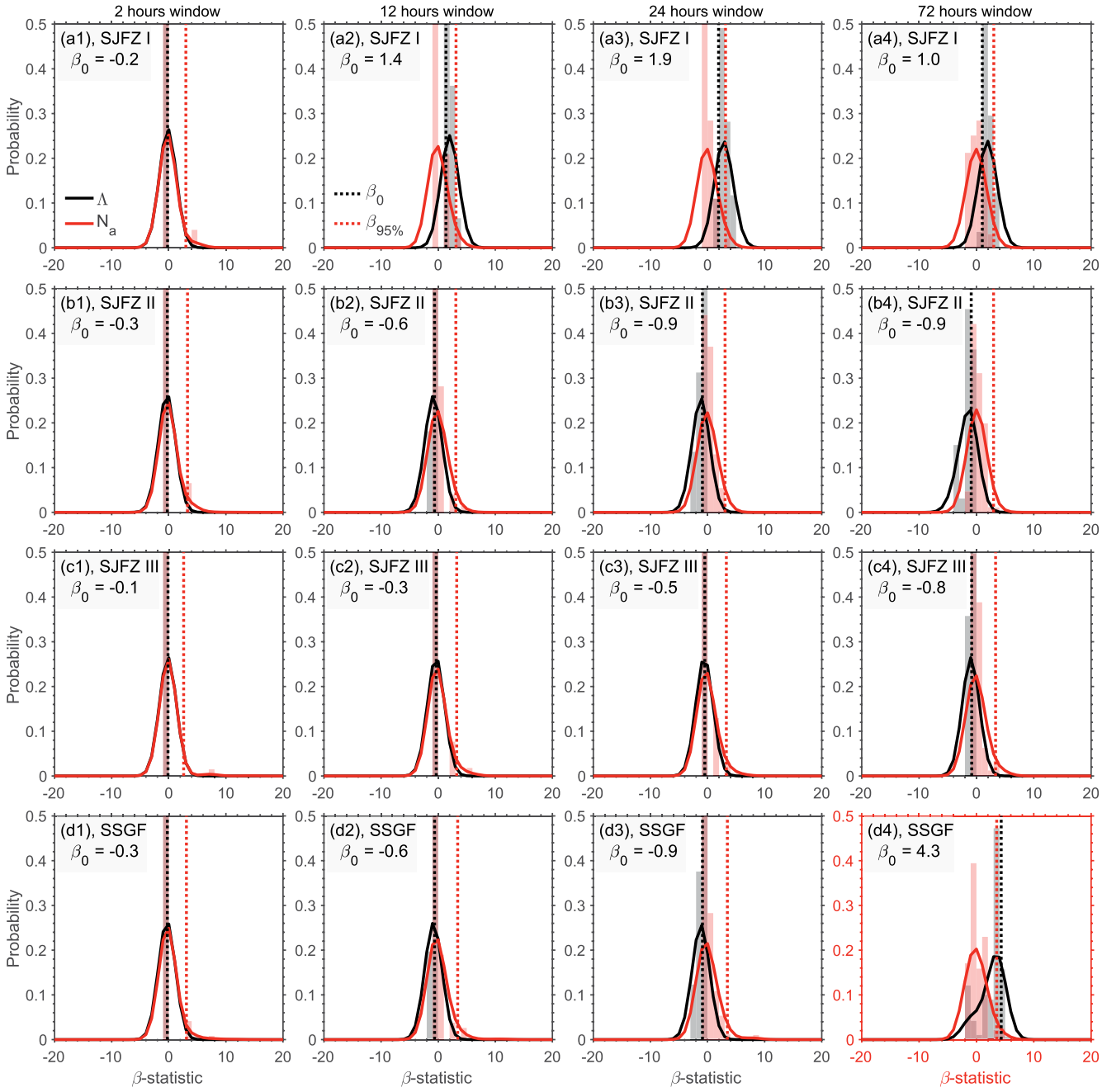

Figure 14. The β-statistic distributions in the SJFZ (a–c) and the SSGF (d) regions after the 2012 M_w 7.8 Haida Gwaii earthquake for local seismicity with $M \geq 1.3$. The legends are similar to those in Figure 2 and Figure 3. The rows represent different regions and the columns represent different time windows.

explain the instantaneously dynamically triggered earthquakes during the passage of the seismic waves, and it also suggests that there should be a peak dynamic stress (strain) threshold for a given region. However, the model cannot fully explain the delayed triggering processes, and a robust PGV (or peak dynamic stress) triggering threshold remains elusive (Freed, 2005; Prejean & Hill, 2015). Such a model would also suggest a scaling relationship between triggering earthquake magnitude and distance, which is less apparent than what numerous studies have found.

Nonlinear triggering models are inherently more complex in comparison to linear triggering models and so can encompass a variety of physical processes (Freed, 2005; Hill & Prejean, 2015). For example, the

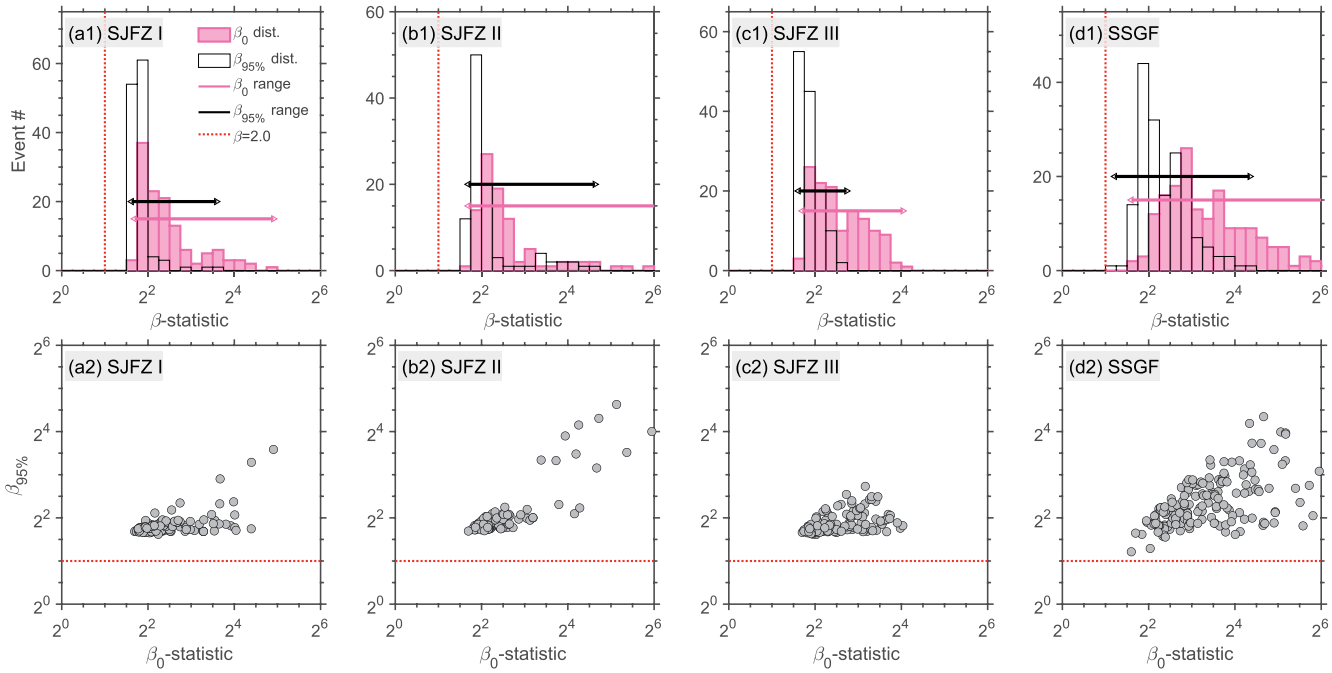

Figure 15. Top row: distributions of the triggering threshold ($\beta_{95\%}$) and the seismicity rate change (β_0) of the triggering cases for SJFZ-I (a), II (b), III (c), and SSGF (d). The horizontal lines show the ranges of the triggering threshold (black line) and the seismicity rate change (pink lines). Bottom row: scatter plot of the triggering threshold ($\beta_{95\%}$) and the seismicity rate change (β_0) of the four regions.

transient strain perturbation may alter the friction leading to an unstable sliding, effectively, triggering an earthquake (Parsons, 2005). Such processes correlate more strongly with wavefield features, including the frequency content of the passing seismic waves and the duration of intense ground motions, more than the peak dynamic strain (Brodsky & Prejean, 2005; Guilhem et al., 2010; Parsons & Velasco, 2009; Pollitz et al., 2012). Other complex nonlinear models may involve multiple physical processes, including stress corrosion, material fatigue, fault gouge modulus reduction, permeability enhancement (pore pressure redistribution), and fluid transportation (Atkinson, 1984; Barbour, 2015; Beeler et al., 2000; Beeler & Lockner, 2003; Ferdowsi et al., 2015; Gomberg et al., 2001; P. A. Johnson & Jia, 2005; Kanamori & Brodsky, 2004; Manga & Brodsky, 2006). The nonlinear physical processes can better explain the commonly observed delayed-dynamic triggering and may also explain some or all of the instantaneously dynamically triggered events (Freed, 2005; Hill & Prejean, 2015).

5.4.1. Instantaneous Triggering

We observe a range of dynamic triggering responses in SJFZ and SSGF, including instantaneous, extended, and delayed triggering (Figure 12). Overall, these observations can be better explained by the nonlinear triggering models. However, we first examine the instantaneously triggered events that could be explained by simple dynamic Coulomb stress changes. For example, microearthquakes were instantaneously dynamically triggered by the 2012 M_w 6.0 Santa Cruz Islands earthquake in SJFZ-I, with a clear change in seismicity that decays rapidly back to background levels (Figure 4). Such a short, transient elevation of seismicity agrees well with the simple linear failure model. However, we find no simple PGV threshold to explain all 55 cases (Figure 5). This observation could suggest that local PGV does not directly correlate with earthquake dynamic triggering. Alternatively, the lack of a clear PGV threshold may be due to a strong spatial variability of PGV triggering thresholds, which might reflect variations in material strength within the fault system.

We find that the PGV values of the triggering earthquakes span five orders of magnitudes in SJFZ-I (Figure 6). Furthermore, the PGV values and wavefields of the "twin" earthquakes are statistically indistinguishable from those of the triggering earthquakes, which further erodes support for triggering being controlled

by dynamic Coulomb failure. However, this apparent lack of triggering from the "twin" earthquakes might be due to out-of-phase seismic cycles of local microearthquake in SJFZ and SSGF. If the triggering earthquake happens to occur at the end of local microearthquake cycles, then the dynamic stress changes may be sufficient to promote an increase in seismicity (Gomberg et al., 1997; Perfettini et al., 2003). The existence of the "twin" nontriggering earthquakes partially supports the microearthquake cycle hypothesis. The lack of a PGV triggering threshold could also be due to insufficient in-situ observations, which may be inadequate to faithfully capture the PGV at the triggered earthquake locations (e.g., C. W. Johnson et al., 2020)

For the SJFZ and SSGF, the instantaneously triggered seismicity can be explained by nonlinear triggering models. Fault strength or frictional properties can be temporarily reduced due to processes initiated by the passing seismic waves, which can lead to either instantaneous or delayed triggering (Savage & Marone, 2008; P. A. Johnson et al., 2008; P. A. Johnson & Jia, 2005). Depending on the local fault states, including the stress states, material strength, and frictional properties, both instantaneous and delayed-dynamic triggering cases may be modulated by the same physical processes. The nonlinear triggering models are also favored because of the diverse triggering PGV values at the same fault system (Figure 5). These nonlinear models do not directly correlate with the peak dynamic strains, therefore a large range of PGV values can produce the observed dynamic triggering cases by these nonlinear models (Prejean & Hill, 2018).

Intriguingly, there are systematic variations in the spectra of ground motions between the instantaneous, extended, and delayed triggering waveforms (Figures 8c and 8d). Such frequency content variation of local ground motions may promote nonlinear triggering processes. Previous studies have documented that long-period seismic waves (≥30 s) are more effective at triggering local seismicity, and frequency-dependent triggering patterns may indicate a porous medium response that initiates fluid flow (e.g., Brodsky & Prejean, 2005; Guilhem et al., 2010; Kane et al., 2007). We observe a clear distinction in the velocity spectra of instantaneously triggering earthquakes in SJFZ-I: relatively strong low-frequency ground motions occurred compared to those that had caused extended or delayed triggering (Figure 8c). We do not see the same pattern in SJFZ-II, although it is unclear whether this discrepancy is due to uneven station coverage in the region (Figures 8b and 8d). There were no stations in the SJFZ-III region, and the station coverage in SSGF is insufficient to make such a comparison.

5.4.2. Delayed Triggering

Perhaps, the most interesting observation is the more frequent occurrence of delayed-dynamic triggering (up to 24 h) compared to instantaneous triggering at all four fault systems (Figure 12). Most of the dynamically triggered earthquakes in SJFZ and SSGF occurred after the passage of the seismic waves, but for different length windows following the triggering event. These delayed-dynamic triggering responses cannot be directly explained by the dynamic Coulomb stress and may have been caused by either multiple different complex nonlinear physical processes occurring simultaneously or the same nonlinear process that evolves on multiple time scales. For example, the 2012 M_w 7.8 Haida Gwaii earthquake caused delayed-dynamic triggering at all fault segments within three days (Figures 2 and 3). However, the triggering responses were not coincident in time, suggesting multiple nonlinear processes may occur simultaneously (e.g., Rivera & Kanamori, 2002). Considering the small spatial footprint of the SJFZ and SSGF, such observations underline that the heterogenous responses are likely controlled by strong spatial heterogeneity of the stress field and/or material properties.

Our results show that it is challenging to characterize the triggering response uniformly: the observed triggering cases occur for a large range of background seismicity rates and incident seismic wave amplitudes in the SJFZ and SSGF regions (Figures 5 and 15). We also do not observe clear triggering-response differences between natural faults (SJFZ) and geothermal reservoirs (SSGF), which suggests that dynamic triggering likely occurs in many fault environments such that geothermal fields are not necessarily more susceptible to dynamic triggering than natural faults. We are unable to determine whether the dominant triggering mechanisms differ from fault to fault. However, the clear spatiotemporal evolutions of the triggering threshold ($\beta_{95\%}$) and the triggered seismicity response (β_0) require the controlling physical mechanisms be time- and space-dependent, with the occurrence of previous earthquakes and slip histories possibly affecting the fault

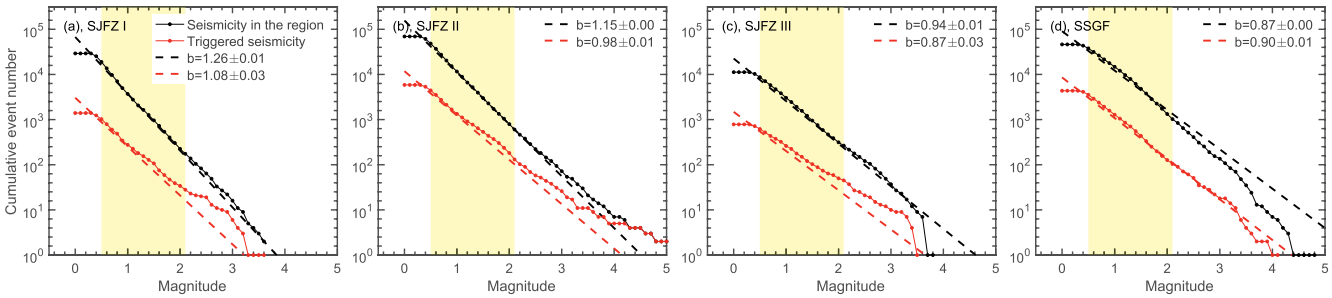

Figure 16. Magnitude-frequency distributions of the triggered earthquake and the background seismicity of the four regions: (a), SJFZ-I, (b), SJFZ-II, (c), SJFZ-III, and (d) SSGF. The yellow patch (M 0.5 to 2.1) shows the magnitude range that is used to estimate the b-value (Aki, 1965).

zone material damage degrees and stress conditions. This means the transient dynamic triggering responses may need to be evaluated within a larger and longer perspective.

5.5. Azimuthal Distributions of the Triggering Earthquakes

The clear higher triggering percentage of earthquakes from back-azimuthal directions of 60°–90° and 180°–210° suggests a preferential triggering pattern (Figure 10). This suggests that incoming wave orientation might be a controlling factor in dynamic triggering of the subregions (Alfaro-Diaz et al., 2020). The azimuthal preferential triggering is likely due to a combination of local fault geometry, stress field orientation, and particle motions of the fault zone materials (Alfaro-Diaz et al., 2020; Gonzalez-Huizar & Velasco, 2011). For example, local SHmax stress is roughly oriented toward NNE at the SJFZ areas and earthquakes from the 60°–90° direction are approximately perpendicular to the direction of the local SHmax stress field (Yang & Hauksson, 2013; Heidbach et al., 2016, 2018), which surface waves could promote dynamic triggering by increasing shearing on the faults (e.g., Alfaro-Diaz et al., 2020; Gonzalez-Huizar & Velasco, 2011). Microearthquakes in the SSGF area are preferably triggered by earthquakes from the 180°–210° direction, parallel to the local SHmax direction (Yang & Hauksson, 2013). These preferential directions might be also due to effects of unclamping faults and effectively reducing friction from the transient waves, which would promote fault slip as well (Gonzalez-Huizar & Velasco, 2011). However, local scale SHmax is highly heterogenous, and such heterogeneities would match a wide range of orientations of the incoming surface waves (Abolfathian et al., 2020; Li et al., 2015; Yang & Hauksson, 2013). Consequentially, earthquakes from all directions can cause dynamic triggering in Southern California (Figure 10). For example, at the SJFZ-I and SJFZ-III segments, the triggering percentage is roughly comparable at different directions (Figure 10). Overall, our observations show that remote earthquakes are more likely to trigger microearthquakes when local SHmax (or SHmin) and fault structures are favorably aligned.

5.6. Depth Distributions of Triggered Microearthquakes

We observe that the depth distribution of triggered earthquakes differs from that of the background seismicity, even though their magnitude-frequency pattens are similar (Figures 16 and 17). To investigate this further, the triggered earthquakes for the three triggering responses (instantaneous, extended, and delayed) are grouped separately for each region, and then compared to the distributions of all events from 2008 to 2017 within a given region, for example, SJFZ-I (Figure 17a). The depth distributions are modeled with kernel probability distributions with a smoothing parameter as $h = 1$, which effectively averages the events with a 1 km depth bin (Figure 17). To understand the variability of the depth distribution, we performed bootstrap resampling on the earthquakes from both the triggered earthquakes and the background seismicity (Figure S2). The triggered earthquake depth distributions are generally different from the distributions of the background earthquakes at all four regions (Figure 17). For example, at SJFZ-I, the instantaneously triggered earthquakes cluster at the base of the seismogenic zone, while the earthquakes triggered after some delay time concentrate at shallower depth (Figure 17a). The triggered earthquake depth distribution

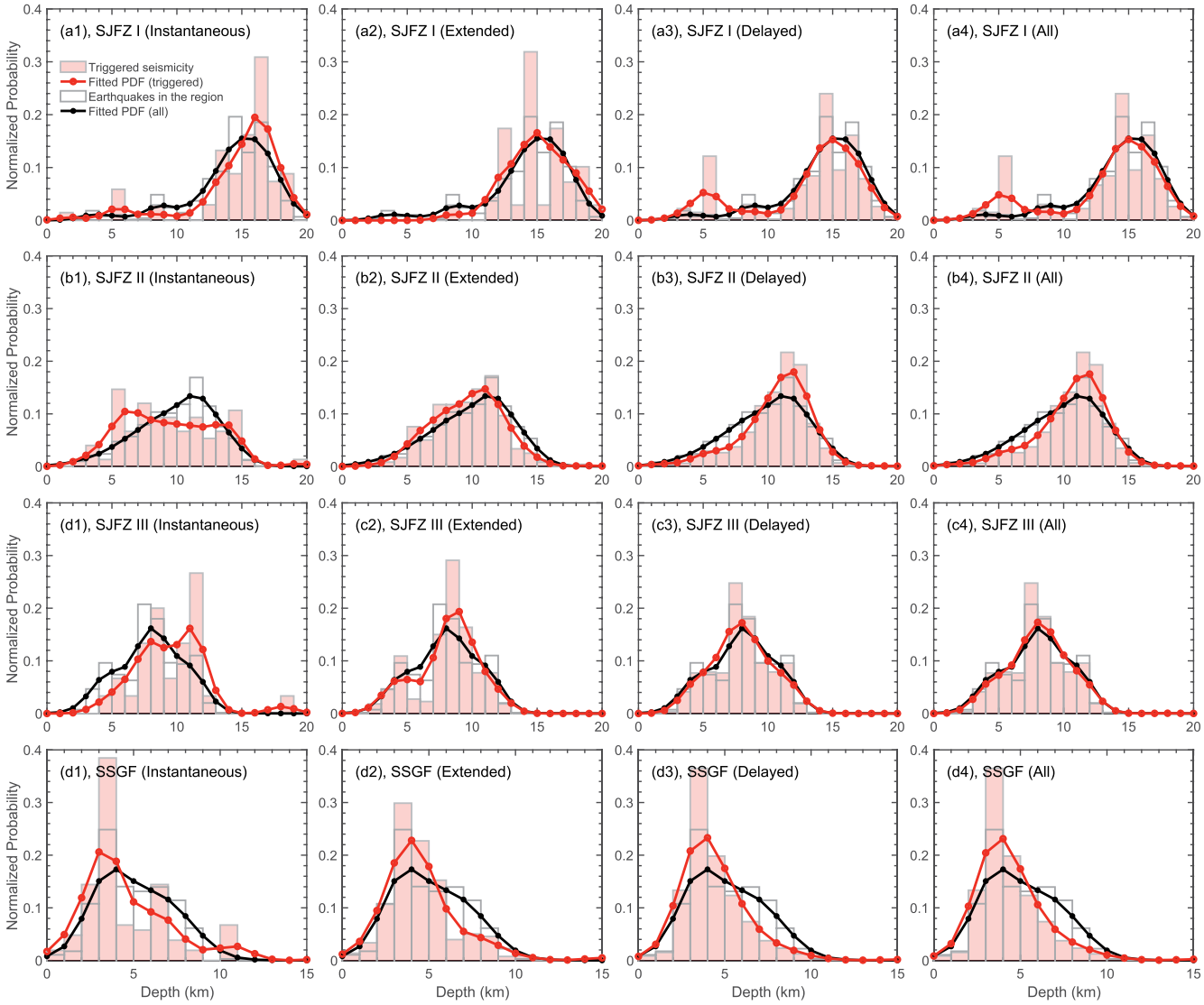

Figure 17. Triggered earthquake depth distributions (red histogram and red curve) and the background seismicity depth distributions (white histogram and black curve) of SJFZ-I (a), II (b), III (c), and SSGF (d). The rows show different regions and the columns show diferent triggering modes.

of SJFZ-I—including all three modes of triggering—shows a concentration of shallow seismicity, which differs from the background seismicity (Figure 17a4).

Depth distributions also differ from region to region. For the SJFZ-III area, the triggered earthquake depth distribution is similar to the background seismicity, although the instantaneously triggered earthquakes tend to occur near the deeper edge of the seismogenic zone, sharing similarities with the distribution of SJFZ-I. At the SSGF, triggered earthquakes consistently concentrate near the shallow edge of the seismogenic zone except the instantaneously triggered earthquake cluster at both edges (Figure 17d). Presumably, the shallow portion of a fault has lower confining stresses, and the triggering thresholds may have scaled with the depth for a given fault (Figure 17).

On the deeper part of the faults, these depth distributions suggest a possible correlation with triggered, transient aseismic creep events that have been measured with seismic and geodetic data (Inbal et al., 2017; Lohman & McGuire, 2007; Tymofyeyeva & Fialko, 2018; Wdowinski, 2009). Transient creeping events can cause an instantaneous or delayed-dynamic triggering of earthquakes or tremor (e.g., Inbal et al., 2017; Shelly et al., 2011), and such creep events might also temporarily alter the effective loading rates, reduc-

ing the earthquake nucleation size significantly (Guérin-Marthe et al., 2019; McLaskey, 2019). The combined effects of reduced nucleation sizes and increased stressing rates from the aseismic events would be effective at promoting microearthquake triggering. Earthquake nucleation length also inversely scales with the initial stress, suggesting an even smaller nucleation size for deep earthquakes during a creeping event (Guérin-Marthe et al., 2019; Latour et al., 2013; McLaskey, 2019). With a smaller nucleation size, these earthquakes would be preferentially triggered if the fracture surface energy scales with the nucleation length (Ide & Aochi, 2005).

Stochastic frictional heterogeneities can also cause microearthquakes preferably triggered at seismogenic zone edges (Lapusta & Rice, 2003; Jiang & Fialko, 2016; Wei et al., 2013). Such frictional heterogeneities often correlate with creep events, which may have contributed collectively at dynamically triggering earthquakes in SJFZ and SSGF. There may be a single, pervasive triggering process that influences the triggering response of these fault segments, but we cannot yet rule out the possibility that multiple nonlinear processes are responsible for the variations in the observed response (Figure 17). The similar magnitude-frequency distributions suggest that once an earthquake is triggered, the following seismicity sequence would tend to the Gutenberg-Richter law and the sequence development likely follows an ETAS-type evolution model (Helmstetter & Sornette, 2002; Ogata, 1999).

6. Conclusions

We develop a new statistical approach to identify earthquake dynamic triggering by evaluating seismicity rate change distributions. This method is data-driven and does not assume seismicity occurrence distributions. By applying the approach to the Quake Template Matching catalog in Southern California from 2008 to 2017, we find the following major points:

1. The commonly used $\beta_0 \geq 2.0$ threshold is insufficient to robustly identify dynamic triggering cases: the β triggering threshold has a wide range of values, shows strong spatial variations, and evolves through time
2. Over 20% of global $M_w \geq 6$ earthquakes, at all depths, triggered microearthquakes in the San Jacinto Fault Zone and the Salton Sea Geothermal Field
3. Distant earthquakes from back-azimuthal directions of 60°–90° and 180°–210° are more likely to trigger earthquakes in Southern California
4. Both instantaneous and delayed-dynamic triggering are seen in these regions; the majority of cases are delayed-dynamic triggering
5. The observed peak ground velocity is not an effective discriminant between triggering earthquakes and nontriggering events. However, the ground motions from earthquakes that caused instantaneous triggering in SJFZ-I are enriched in low-frequency energy compared to those associated with extended or delayed triggering
6. There are significant spatial and temporal variations in triggering response, and differences between the depth distributions of triggered and background seismicity

These observations suggest highly heterogeneous local stress states and material strength and also suggest triggering mechanisms are not invariant but rather a continuously evolving processes. They also suggest that while linear dynamic triggering mechanisms may have contributed to the observed instantaneous triggering, nonlinear physical processes may dominate the triggering processes. For example, dynamic strains may trigger aseismic creep processes and/or alter frictional strength, which eventually trigger the local earthquakes. This interpretation is supported by the observation that the triggered events concentrate at the edges of the seismogenic zones, especially at shallow depths.

Data Availability Statement

The earthquake catalogs used in this study are from the Global Centroid Moment Tensor project (Ekström et al., 2012) and the Southern California Earthquake Data Center (QTM catalog) (Ross et al., 2019). The seismic data were provided by Data Management Center (DMC) of the Incorporated Research Institutions

for Seismology (IRIS). The facilities of IRIS Data Services, and specifically the IRIS Data Management Center, were used for access to waveforms, related metadata, and/or derived products used in this study. IRIS Data Services are funded through the Seismological Facilities for the Advancement of Geoscience and EarthScope (SAGE) Proposal of the National Science Foundation (NSF) under Cooperative Agreement EAR-1261681. Network of the Americas (NOTA) strain data were also obtained from the IRIS DMC; this material is based on services provided by the GAGE Facility, operated by UNAVCO, Inc., with support from the NSF and the National Aeronautics and Space Administration (NASA) under NSF Cooperative Agreement EAR-1724794. The triggering earthquakes and their associated "twin" earthquakes are listed in the Supporting Information.

Acknowledgments
We would like to thank the editor Dr. Abercrombie, the Associate Editor, Dr. Gomberg, Dr. Prejean, Dr. Kilb, and the two reviewers for their constructive suggestions. Wenyuan Fan was supported by NSF EAR-2022441. Guoqing Lin was supported by NSF EAR-2022429. Any use of trade, firm, or product names is for descriptive purposes only and does not imply endorsement by the US government.

References

Abolfathian, N., Martínez-Garzón, P., & Ben-Zion, Y. (2020). Variations of stress parameters in the Southern California plate boundary around the South Central Transverse Ranges. *Journal of Geophysical Research: Solid Earth*, *125*(8). https://doi.org/10.1029/2020jb019482

Agnew, D. C., & Wyatt, F. K. (2014). Dynamic strains at regional and teleseismic distances. *Bulletin of the Seismological Society of America*, *104*(4), 1846–1859. https://doi.org/10.1785/0120140007

Aiken, C., Meng, X., & Hardebeck, J. (2018). Testing for the 'predictability' of dynamically triggered earthquakes in the Geysers geothermal field. *Earth and Planetary Science Letters*, *485*, 129–140. https://doi.org/10.1016/j.epsl.2018.01.015

Aiken, C., Peng, Z., & Chao, K. (2013). Tremors along the Queen Charlotte margin triggered by large teleseismic earthquakes. *Geophysical Research Letters*, *40*(5), 829–834. https://doi.org/10.1002/grl.50220

Aki, K. (1965). Maximum likelihood estimate of b in the formula log N=a-bM and its confidence limits. *Bulletin of Earthquake Research Institute of the University of Tokyo*, *43*, 237–239.

Alfaro-Diaz, R., Velasco, A. A., Pankow, K. L., & Kilb, D. (2020). Optimally Oriented Remote Triggering in the Coso Geothermal Region. *Journal of Geophysical Research: Solid Earth*, *125*(8). http://dx.doi.org/10.1029/2019jb019131

Aron, A., & Hardebeck, J. L. (2009). Seismicity Rate Changes along the Central California Coast due to Stress Changes from the 2003 M 6.5 San Simeon and 2004 M 6.0 Parkfield Earthquakes. *Bulletin of the Seismological Society of America*, *99*(4), 2280–2292. http://dx.doi.org/10.1785/0120080239

Atkinson, B. K. (1984). Subcritical crack growth in geological materials. *Journal of Geophysical Research: Solid Earth*, *89*(B6), 4077–4114. http://dx.doi.org/10.1029/jb089ib06p04077

Barbour, A. J. (2015). Pore pressure sensitivities to dynamic strains: Observations in active tectonic regions. *Journal of Geophysical Research: Solid Earth*, *120*(8), 5863–5883. http://dx.doi.org/10.1002/2015jb012201

Barbour, A. J., & Agnew, D. C. (2012). Detection of seismic signals using seismometers and strainmeters. *Bulletin of the Seismological Society of America*, *102*(6), 2484–2490. https://doi.org/10.1785/0120110298

Barbour, A. J., & Parker, R. L. (2014). psd: Adaptive, sine multitaper power spectral density estimation for r. *Computers & Geosciences*, *63*, 1–8. https://doi.org/10.1002/2015jb012201

Beeler, N. M. (2003). Why earthquakes correlate weakly with the solid Earth tides: Effects of periodic stress on the rate and probability of earthquake occurrence. *Journal of Geophysical Research*, *108*(B8). http://dx.doi.org/10.1029/2001jb001518

Beeler, N. M., Simpson, R. W., Hickman, S. H., & Lockner, D. A. (2000). Pore fluid pressure, apparent friction, and Coulomb failure. *Journal of Geophysical Research*, *105*(B11), 25533–25542. https://doi.org/10.1029/2000JB900119

Bowman, A. W., & Azzalini, A. (1997). Applied smoothing techniques for data analysis: The kernel approach with S-Plus illustrations (Vol. 18). Oxford, England: OUP.

Brodsky, E. E. (2006). Long-range triggered earthquakes that continue after the wave train passes. *Geophysical Research Letters*, *33*(15). https://doi.org/10.1029/2006gl026605

Brodsky, E. E., & Lajoie, L. J. (2013). Anthropogenic seismicity rates and operational parameters at the Salton Sea Geothermal Field. *Science*, *341*(6145), 543–546. https://doi.org/10.1126/science.1239213

Brodsky, E. E., & Prejean, S. G. (2005). New constraints on mechanisms of remotely triggered seismicity at Long Valley caldera. *Journal of Geophysical Research*, *110*(B4). https://doi.org/10.1029/2004jb003211

Brodsky, E. E. (2003). A mechanism for sustained groundwater pressure changes induced by distant earthquakes. *Journal of Geophysical Research*, *108*(B8). http://dx.doi.org/10.1029/2002jb002321

Cai, C., & Wiens, D. A. (2016). Dynamic triggering of deep earthquakes within a fossil slab. *Geophysical Research Letters*, *43*(18), 9492–9499. https://doi.org/10.1002/2016gl070347

Cattania, C., McGuire, J. J., & Collins, J. A. (2017). Dynamic triggering and earthquake swarms on East Pacific Rise transform faults. *Geophysical Research Letters*, *44*(2), 702–710. http://dx.doi.org/10.1002/2016gl070857

Cheng, Y., & Chen, X. (2018). Characteristics of seismicity inside and outside the Salton Sea Geothermal Field. *Bulletin of the Seismological Society of America*, *108*(4), 1877–1888. http://dx.doi.org/10.1785/0120170311

Chen, X., & Shearer, P. M. (2011). Comprehensive analysis of earthquake source spectra and swarms in the Salton Trough, California. *Journal of Geophysical Research*, *116*(B9). https://doi.org/10.1029/2011JB008263

Crandall-Bear, A., Barbour, A. J., & Schoenball, M. (2018). *Irregular focal mechanisms observed at Salton Sea Geothermal Field: Possible influences of anthropogenic stress perturbations*. Paper presented at 43rd Workshop on Geothermal Reservoir Engineering.

Delbridge, B. G., Kita, S., Uchida, N., Johnson, C. W., Matsuzawa, T., & Bürgmann, R. (2017). Temporal variation of intermediate-depth earthquakes around the time of the M9. 0 Tohoku-oki earthquake. *Geophysical Research Letters*, *44*(8), 3580–3590. http://dx.doi.org/10.1002/2017gl072876

Ekström, G., Nettles, M., & Dziewoński, A. M. (2012). The global CMT project 2004–2010: Centroid-moment tensors for 13,017 earthquakes. *Physics of the Earth and Planetary Interiors*, *200-201*, 1–9. http://dx.doi.org/10.1016/j.pepi.2012.04.002

Fan, W., & Shearer, P. M. (2016). Local near instantaneously dynamically triggered aftershocks of large earthquakes. *Science*, *353*(6304), 1133–1136. http://dx.doi.org/10.1002/2017jb014495

Fan, W., & Shearer, P. M. (2017). Investigation of backprojection uncertainties with M6 earthquakes. *Journal of Geophysical Research: Solid Earth*, *122*(10), 7966–7986. http://dx.doi.org/10.1002/2017jb014495
Fan, W., Wei, S. S., Tian, D., McGuire, J. J., & Wiens, D. A. (2019). Complex and diverse rupture processes of the 2018 Mw 8.2 and Mw 7.9 Tonga-Fiji deep earthquakes. *Geophysical Research Letters*, *46*(5), 2434–2448. http://dx.doi.org/10.1029/2018gl080997
Ferdowsi, B., Griffa, M., Guyer, R. A., Johnson, P. A., Marone, C., & Carmeliet, J. (2015). Acoustically induced slip in sheared granular layers: Application to dynamic earthquake triggering. *Geophysical Research Letters*, *42*(22), 9750–9757. http://dx.doi.org/10.1002/2015gl066096
Freed, A. M. (2005). Earthquake triggering by static, dynamic, and postseismic stress transfer. *Annual Review of Earth and Planetary Sciences*, *33*, 335–367. http://dx.doi.org/10.1146/annurev.earth.33.092203.122505
Gomberg, J., Blanpied, M. L., & Beeler, N. (1997). Transient triggering of near and distant earthquakes. *Bulletin of the Seismological Society of America*, *87*(2), 294–309.
Gomberg, J., & Johnson, P. (2005). Seismology: Dynamic triggering of earthquakes. *Nature*, *437*(7060), 830. http://dx.doi.org/10.1038/437830a
Gomberg, J., Reasenberg, P. A., Bodin, P., & Harris, R. A. (2001). Earthquake triggering by seismic waves following the Landers and Hector Mine earthquakes. *Nature*, *411*(6836), 462–466. http://dx.doi.org/10.1038/35078053
Gonzalez-Huizar, H., & Velasco, A. A. (2011). Dynamic triggering: Stress modeling and a case study. *Journal of Geophysical Research*, *116*(B2). http://dx.doi.org/10.1029/2009jb007000
Gonzalez-Huizar, H., Velasco, A. A., Peng, Z., & Castro, R. R. (2012). Remote triggered seismicity caused by the 2011, M9. 0 Tohoku-oki, Japan earthquake. *Geophysical Research Letters*, *39*(10). https://doi.org/10.1029/2012GL051015
Guérin-Marthe, S., Nielsen, S., Bird, R., Giani, S., & Di Toro, G. (2019). Earthquake nucleation size: Evidence of loading rate dependence in laboratory faults. *Journal of Geophysical Research: Solid Earth*, *124*(1), 689–708. http://dx.doi.org/10.1029/2018jb016803
Guilhem, A., Peng, Z., & Nadeau, R. M. (2010). High-frequency identification of non-volcanic tremor triggered by regional earthquakes. *Geophysical Research Letters*, *37*(16). http://dx.doi.org/10.1029/2010gl044660
Habermann, R. E. (1987). Man-made changes of seismicity rates. *Bulletin of the Seismological Society of America*, *77*(1), 141–159.
Hanks, T. C., & Kanamori, H. (1979). A moment magnitude scale. *Journal of Geophysical Research*, *84*(B5), 2348–2350. https://doi.org/10.1029/JB084iB05p02348
Harrington, R. M., & Brodsky, E. E. (2006). The absence of remotely triggered seismicity in Japan. *Bulletin of the Seismological Society of America*, *96*(3), 871–878. http://dx.doi.org/10.1785/0120050076
Harris, R. A. (1998), Introduction to special section: Stress triggers, stress shadows, and implications for seismic hazard. *Journal of Geophysical Research*, *103*(B10), 24347–24358. https://doi.org/10.1029/98JB01576
Harris, R. A. (2002). The 1999 Izmit, Turkey, Earthquake: A 3D Dynamic Stress Transfer Model of Intraearthquake Triggering. *Bulletin of the Seismological Society of America*, *92*(1), 245–255. http://dx.doi.org/10.1785/0120000825
Heidbach, O., Rajabi, M., Cui, X., Fuchs, K., Müller, B., Reinecker, J., et al. (2018). The World Stress Map database release 2016: Crustal stress pattern across scales. *Tectonophysics*, *744*, 484–498. http://dx.doi.org/10.1016/j.tecto.2018.07.007
Heidbach, O., Rajabi, M., Reiter, K., Ziegler, M., Team, W., et al. (2016). World stress map database release 2016 (Vol. 10): GFZ Data Services. http://dx.doi.org/10.5880/WSM.2016.001
Helmstetter, A., & Sornette, D. (2002). Diffusion of epicenters of earthquake aftershocks, Omori's law, and generalized continuous-time random walk models. *Physical Review E*, *66*(6), 061104. http://dx.doi.org/10.1103/physreve.66.061104
Hill, D. P. (2008). Dynamic stresses, Coulomb failure, and remote triggering. *Bulletin of the Seismological Society of America*, *98*(1), 66–92. http://dx.doi.org/10.1785/0120070049
Hill, D. P., Reasenberg, P., Michael, A., Arabaz, W., Beroza, G., Brumbaugh, D., et al. (1993). Seismicity remotely triggered by the magnitude 7.3 Landers, California, earthquake. *Science*, *260*(5114), 1617–1623. http://dx.doi.org/10.1126/science.260.5114.1617
Ide, S., & Aochi, H. (2005). Earthquakes as multiscale dynamic ruptures with heterogeneous fracture surface energy. *Journal of Geophysical Research*, *110*(B11). http://dx.doi.org/10.1029/2004jb003591
Inbal, A., Ampuero, J.-P., & Avouac, J.-P. (2017). Locally and remotely triggered aseismic slip on the central San Jacinto fault near Anza, CA, from joint inversion of seismicity and strainmeter data. *Journal of Geophysical Research: Solid Earth*, *122*(4), 3033–3061. http://dx.doi.org/10.1002/2016jb013499
Jiang, J., & Fialko, Y. (2016). Reconciling seismicity and geodetic locking depths on the Anza section of the San Jacinto fault. *Geophysical Research Letters*, *43*(20), 10–663. http://dx.doi.org/10.1002/2016gl071113
Johnson, H. P., Gomberg, J. S., Hautala, S. L., & Salmi, M. S. (2017). Sediment gravity flows triggered by remotely generated earthquake waves. *Journal of Geophysical Research: Solid Earth*, *122*(6), 4584–4600. http://dx.doi.org/10.1002/2016jb013689
Johnson, P. A., & Jia, X. (2005). Nonlinear dynamics, granular media and dynamic earthquake triggering. *Nature*, *437*(7060), 871. http://dx.doi.org/10.1038/nature04015
Johnson, C. W., Kilb, D., Baltay, A., & Vernon, F. (2020). Peak ground velocity spatial variability revealed by dense seismic array in Southern California. *Journal of Geophysical Research: Solid Earth*, e2019JB019157. http://dx.doi.org/10.1029/2019jb019157
Johnson, P. A., Savage, H., Knuth, M., Gomberg, J., & Marone, C. (2008). Effects of acoustic waves on stick–slip in granular media and implications for earthquakes. *Nature*, *451*(7174), 57. http://dx.doi.org/10.1038/nature06440
Kanamori, H., & Brodsky, E. E. (2004). The physics of earthquakes. *Reports on Progress in Physics*, *67*(8), 1429. http://dx.doi.org/10.1088/0034-4885/67/8/r03
Kane, D. L., Kilb, D., Berg, A. S., & Martynov, V. G. (2007). Quantifying the remote triggering capabilities of large earthquakes using data from the Anza Seismic Network catalog (Southern California). *Journal of Geophysical Research*, *112*(B11). http://dx.doi.org/10.1029/2006jb004714
Kaven, J. O. (2020). Seismicity rate change at the Coso Geothermal Field following the July 2019 Ridgecrest Earthquakes. *Bulletin of the Seismological Society of America*. https://doi.org/10.1785/0120200017
Kennett, B., & Engdahl, E. (1991). Traveltimes for global earthquake location and phase identification. *Geophysical Journal International*, *105*(2), 429–465. http://dx.doi.org/10.1111/j.1365-246x.1991.tb06724.x
Kilb, D. (2003). A strong correlation between induced peak dynamic Coulomb stress change from the 1992 M7. 3 Landers, California, earthquake and the hypocenter of the 1999 M7. 1 Hector Mine, California, earthquake. *Journal of Geophysical Research*, *108*(B1), ESE–3. http://dx.doi.org/10.1029/2001jb000678
Kilb, D., Gomberg, J., & Bodin, P. (2000). Triggering of earthquake aftershocks by dynamic stresses. *Nature*, *408*(6812), 570. http://dx.doi.org/10.1038/35046046
King, G. C. P., Stein, R. S., & Lin, J. (1994). Static stress changes and the triggering of earthquakes. *Bulletin of the Seismological Society of America*, *84*(3), 935–953.

Lapusta, N., & Rice, J. R. (2003). Nucleation and early seismic propagation of small and large events in a crustal earthquake model. *Journal of Geophysical Research*, *108*(B4). http://dx.doi.org/10.1029/2001jb000793
Latour, S., Schubnel, A., Nielsen, S., Madariaga, R., & Vinciguerra, S. (2013). Characterization of nucleation during laboratory earthquakes. *Geophysical Research Letters*, *40*(19), 5064–5069. http://dx.doi.org/10.1002/grl.50974
Li, Z., Peng, Z., Ben-Zion, Y., & Vernon, F. L. (2015). Spatial variations of shear wave anisotropy near the San Jacinto Fault Zone in Southern California. *Journal of Geophysical Research: Solid Earth*, *120*(12), 8334–8347. http://dx.doi.org/10.1002/2015jb012483
Llenos, A. L., & Michael, A. J. (2016). Characterizing potentially induced earthquake rate changes in the Brawley Seismic Zone, Southern California. *Bulletin of the Seismological Society of America*, *106*(5), 2045–2062. https://doi.org/10.1785/0120150053
Lohman, R., & McGuire, J. (2007). Earthquake swarms driven by aseismic creep in the Salton Trough, California. *Journal of Geophysical Research*, *112*(B4). http://dx.doi.org/10.1029/2006jb004596
Luo, Y., & Wiens, D. A. (2020). High rates of deep earthquake dynamic triggering in the thermal halos of subducting slabs. *Geophysical Research Letters*, e2019GL086125. http://dx.doi.org/10.1029/2019gl086125
Manga, M., & Brodsky, E. (2006). Seismic triggering of eruptions in the far field: Volcanoes and geysers. *Annual Review of Earth and Planetary Sciences*, *34*, 263–291. http://dx.doi.org/10.1146/annurev.earth.34.031405.125125
Marsan, D. (2003). Triggering of seismicity at short timescales following Californian earthquakes. *Journal of Geophysical Research: Solid Earth*, *108*(B5). http://dx.doi.org/10.1029/2002jb001946
Marsan, D., & Nalbant, S. S. (2005). Methods for measuring seismicity rate changes: A review and a study of how the Mw 7.3 Landers earthquake affected the aftershock sequence of the Mw 6.1 Joshua Tree earthquake. *Pure and Applied Geophysics*, *162*(6–7), 1151–1185. http://dx.doi.org/10.1007/s00024-004-2665-4
Marsan, D., & Wyss, M. (2011). *Seismicity rate changes*. Community Online Resource for Statistical Seismicity Analysis. http://dx.doi.org/10.5078/corssa-25837590
Matthews, M. V., & Reasenberg, P. A. (1988). Statistical methods for investigating quiescence and other temporal seismicity patterns. *Pure and Applied Geophysics*, *126*(2–4), 357–372. http://dx.doi.org/10.1007/bf00879003
McFadden, D. (1978). *Modeling the choice of residential location*, ISSN: 0361-1981: (Transportation Research Record, 673).Transportation Research Board.
McLaskey, G. C. (2019). Earthquake Initiation From Laboratory Observations and Implications for Foreshocks. *Journal of Geophysical Research: Solid Earth*, *124*(12), 12882–12904. http://dx.doi.org/10.1029/2019jb018363
Meng, X., & Peng, Z. (2014). Seismicity rate changes in the Salton Sea Geothermal Field and the San Jacinto fault zone after the 2010 Mw 7.2 El Mayor-cucapah earthquake. *Geophysical Journal International*, *197*(3), 1750–1762. http://dx.doi.org/10.1093/gji/ggu085
Myers, S. C., Wallace, T. C., Beck, S. L., Silver, P. G., Zandt, G., Vandecar, J., &(1995). Implications of spatial and temporal development of the aftershock sequence for the Mw 8.3 June 9, 1994 deep Bolivian earthquake. *Geophysical Research Letters*, *22*(16), 2269–2272. http://dx.doi.org/10.1029/95gl01600
Nissen, E., Elliott, J., Sloan, R., Craig, T., Funning, G., Hutko, A., et al. (2016). Limitations of rupture forecasting exposed by instantaneously triggered earthquake doublet. *Nature Geoscience*, *9*(4), 330. http://dx.doi.org/10.1038/ngeo2653
Obara, K. (2002). Nonvolcanic deep tremor associated with subduction in southwest Japan. *Science*, *296*(5573), 1679–1681. https://doi.org/10.1126/science.1070378
Ogata, Y. (1999). Seismicity analysis through point-process modeling: A review. In *Seismicity patterns, their statistical significance and physical meaning* (471–507): Springer. https://doi.org/10.1007/978-3-0348-8677-2_14
Pankow, K. L., & Kilb, D. (2020). Going beyond rate changes as the sole indicator for dynamic triggering of earthquakes. *Scientific Reports*, *10*(1), 1–12. http://dx.doi.org/10.1038/s41598-020-60988-2
Parsons, T. (2005). A hypothesis for delayed dynamic earthquake triggering. *Geophysical Research Letters*, *32*(4). http://dx.doi.org/10.1029/2004gl021811
Parsons, T., & Velasco, A. A. (2009). On near-source earthquake triggering. *Journal of Geophysical Research*, *114*(B10). http://dx.doi.org/10.1029/2008jb006277
Peña Castro, A. F., Dougherty, S. L., Harrington, R. M., & Cochran, E. S. (2019). Delayed Dynamic Triggering of Disposal-Induced Earthquakes Observed by a Dense Array in Northern Oklahoma. *Journal of Geophysical Research: Solid Earth*, *124*(4), 3766–3781. http://dx.doi.org/10.1029/2018jb017150
Peng, Z., Vidale, J. E., Wech, A. G., Nadeau, R. M., & Creager, K. C. (2009). Remote triggering of tremor along the San Andreas fault in central California. *Journal of Geophysical Research*, *114*(B7). http://dx.doi.org/10.1029/2008jb006049
Peng, Z., Walter, J. I., Aster, R. C., Nyblade, A., Wiens, D. A., & Anandakrishnan, S. (2014). Antarctic icequakes triggered by the 2010 Maule earthquake in Chile. *Nature Geoscience*, *7*(9), 677. http://dx.doi.org/10.1038/ngeo2212
Peng, Z., Wu, C., & Aiken, C. (2011). Delayed triggering of microearthquakes by multiple surface waves circling the earth. *Geophysical Research Letters*, *38*(4). http://dx.doi.org/10.1029/2010gl046373
Perfettini, H., Schmittbuhl, J., & Cochard, A. (2003). Shear and normal load perturbations on a two-dimensional continuous fault: 2. dynamic triggering. *Journal of Geophysical Research*, *108*(B9). http://dx.doi.org/10.1029/2002jb001805
Plesch, A., Shaw, J. H., Benson, C., Bryant, W. A., Carena, S., Cooke, M., et al. (2007). Community fault model (CFM) for Southern California. *Bulletin of the Seismological Society of America*, *97*(6), 1793–1802. http://dx.doi.org/10.1785/0120050211
Pollitz, F. F., Stein, R. S., Sevilgen, V., & Bürgmann, R. (2012). The 11 April 2012 east Indian Ocean earthquake triggered large aftershocks worldwide. *Nature*, *490*(7419), 250–253. http://dx.doi.org/10.1038/nature11504
Hill, D. P., & Prejean, S.G. (2015). Dynamic Triggering. G. Schubert In *Treatise on Geophysics (Second Edition)* (pp. 273–304). ISBN 9780444538031: Elsevier. https://doi.org/10.1016/B978-0-444-53802-4.00078-6
Prejean, S. G., & Hill, D. P. (2018). The influence of tectonic environment on dynamic earthquake triggering: A review and case study on Alaskan volcanoes. *Tectonophysics*, *745*, 293–304. http://dx.doi.org/10.1016/j.tecto.2018.08.007
Prejean, S. G., Hill, D., Brodsky, E., Hough, S., Johnston, M., Malone, S., et al. (2004). Remotely triggered seismicity on the united states west coast following the Mw 7.9 Denali fault earthquake. *Bulletin of the Seismological Society of America*, *94*(6B), S348–S359. http://dx.doi.org/10.1785/0120040610
Prieto, G., Parker, R., Thomson, D., Vernon, F., & Graham, R. (2007). Reducing the bias of multitaper spectrum estimates. *Geophysical Journal International*, *171*(3), 1269–1281. http://dx.doi.org/10.1111/j.1365-246x.2007.03592.x
Rivera, L., & Kanamori, H. (2002). Spatial heterogeneity of tectonic stress and friction in the crust. *Geophysical Research Letters*, *29*(6), 12–1. http://dx.doi.org/10.1029/2001gl013803
Ross, Z. E., Trugman, D. T., Hauksson, E., & Shearer, P. M. (2019). Searching for hidden earthquakes in Southern California. *Science*, *364*(6442), 767–771. http://dx.doi.org/10.1126/science.aaw6888

Savage, H. M., & Marone, C. (2008). Potential for earthquake triggering from transient deformations. *Journal of Geophysical Research*, *113*(B5). http://dx.doi.org/10.1029/2007jb005277

Shelly, D. R., Peng, Z., Hill, D. P., & Aiken, C. (2011). Triggered creep as a possible mechanism for delayed dynamic triggering of tremor and earthquakes. *Nature Geoscience*, *4*(6), 384–388. http://dx.doi.org/10.1038/ngeo1141

Silverman, B. W. (1986). Density estimation for statistics and data analysis (Vol. 26). CRC press.

Stein, R. S. (1999). The role of stress transfer in earthquake occurrence. *Nature*, *402*(6762), 605–609. http://dx.doi.org/10.1038/45144

Tibi, R., Wiens, D. A., & Inoue, H. (2003). Remote triggering of deep earthquakes in the 2002 tonga sequences. *Nature*, *424*(6951), 921. http://dx.doi.org/10.1038/nature01903

Tymofyeyeva, E., & Fialko, Y. (2018). Geodetic evidence for a blind fault segment at the southern end of the San Jacinto fault zone. *Journal of Geophysical Research: Solid Earth*, *123*(1), 878–891. http://dx.doi.org/10.1002/2017jb014477

Tymofyeyeva, E., Fialko, Y., Jiang, J., Xu, X., Sandwell, D., Bilham, R., et al. (2019). Slow slip event on the southern San Andreas fault triggered by the 2017 Mw 8.2 Chiapas (Mexico) earthquake. *Journal of Geophysical Research: Solid Earth*, *124*(9), 9956–9975. http://dx.doi.org/10.1029/2018jb016765

van Der Elst, N. J., & Brodsky, E. E. (2010). Connecting near-field and far-field earthquake triggering to dynamic strain. *Journal of Geophysical Research*, *115*(B7). http://dx.doi.org/10.1029/2009jb006681

van der Elst, N. J., Savage, H. M., Keranen, K. M., & Abers, G. A. (2013). Enhanced remote earthquake triggering at fluid-injection sites in the midwestern United States. *Science*, *341*(6142), 164–167. http://dx.doi.org/10.1126/science.1238948

Velasco, A. A. (2004). Rupture Directivity of the 3 November 2002 Denali Fault Earthquake Determined from Surface Waves. *Bulletin of the Seismological Society of America*, *94*(6B), S293–S299. http://dx.doi.org/10.1785/0120040624

Velasco, A. A., Hernandez, S., Parsons, T., & Pankow, K. (2008). Global ubiquity of dynamic earthquake triggering. *Nature Geoscience*, *1*(6), 375–379. http://dx.doi.org/10.1038/ngeo204

Wallace, L. M., Kaneko, Y., Hreinsdóttir, S., Hamling, I., Peng, Z., Bartlow, N., et al. (2017). Large-scale dynamic triggering of shallow slow slip enhanced by overlying sedimentary wedge. *Nature Geoscience*, *10*(10), 765. http://dx.doi.org/10.1038/ngeo3021

Wdowinski, S. (2009). Deep creep as a cause for the excess seismicity along the San Jacinto fault. *Nature Geoscience*, *2*(12), 882–885. http://dx.doi.org/10.1038/ngeo684

Wei, M., Kaneko, Y., Liu, Y., & McGuire, J. J. (2013). Episodic fault creep events in California controlled by shallow frictional heterogeneity. *Nature Geoscience*, *6*(7), 566–570. http://dx.doi.org/10.1038/ngeo1835

Yang, W., & Hauksson, E. (2013). The tectonic crustal stress field and style of faulting along the Pacific North America plate boundary in Southern California. *Geophysical Journal International*, *194*(1), 100–117. http://dx.doi.org/10.1093/gji/ggt113

Yun, N., Zhou, S., Yang, H., Yue, H., & Zhao, L. (2019). Automated detection of dynamic earthquake triggering by the high-frequency power integral ratio. *Geophysical Research Letters*, *46*(22), 12977–12985. http://dx.doi.org/10.1029/2019gl083913

Zhang, Q., Lin, G., Zhan, Z., Chen, X., Qin, Y., & Wdowinski, S. (2017). Absence of remote earthquake triggering within the Coso and Salton Sea geothermal production fields. *Geophysical Research Letters*, *44*(2), 726–733. http://dx.doi.org/10.1002/2016gl071964